

NASA  
Technical  
Paper  
3073

May 1991

Computational Methods  
for Frictionless Contact  
With Application to  
Space Shuttle Orbiter  
Nose-Gear Tires

S  
Kyun O. Kim,  
John A. Tanner,  
Ahmed K. Noor,  
and Martha P. Robinson

DISTRIBUTION STATEMENT A  
Approved for public release  
Distribution Unlimited

19960506 019

DTIC QUALITY INSPECTED 1

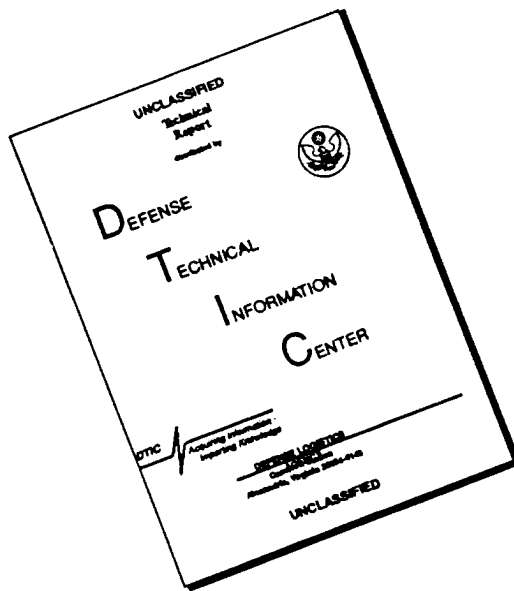
DEPARTMENT OF DEFENCE  
PLASTICS TECHNICAL EVALUATION CENTER  
ARDEC PICATINNY ARSENAL, N.J. 07806

NASA

PLASTEC 055545

Sh 45

# **DISCLAIMER NOTICE**



**THIS DOCUMENT IS BEST  
QUALITY AVAILABLE. THE COPY  
FURNISHED TO DTIC CONTAINED  
A SIGNIFICANT NUMBER OF  
PAGES WHICH DO NOT  
REPRODUCE LEGIBLY.**

**NASA  
Technical  
Paper  
3073**

1991

# Computational Methods for Frictionless Contact With Application to Space Shuttle Orbiter Nose-Gear Tires

Kyun O. Kim

*George Washington University*

*Joint Institute for Advancement of Flight Sciences*

*Langley Research Center*

*Hampton, Virginia*

John A. Tanner

*Langley Research Center*

*Hampton, Virginia*

Ahmed K. Noor

*Center for Computational Structures Technology*

*University of Virginia*

*Langley Research Center*

*Hampton, Virginia*

Martha P. Robinson

*Langley Research Center*

*Hampton, Virginia*



National Aeronautics and  
Space Administration

Office of Management

Scientific and Technical  
Information Division

## Summary

A computational procedure is presented for the solution of frictionless contact problems of aircraft tires. The Space Shuttle orbiter nose-gear tire is modeled using a two-dimensional laminated anisotropic shell theory with the effects of variation in material and geometric parameters, transverse shear deformation, and geometric nonlinearities included. The contact conditions are incorporated into the formulation by using a perturbed Lagrangian approach with the fundamental unknowns consisting of the stress resultants, the generalized displacements, and the Lagrange multipliers associated with the contact conditions. The elemental arrays are obtained by using a modified two-field, mixed variational principle.

Numerical results are presented for the Space Shuttle nose-gear tire inflated and pressed against a flat plate. Comparison is made with experiments conducted at NASA Langley Research Center. The detailed information presented herein assists in gaining insight into the structural response of the tire. The numerical studies have demonstrated the high accuracy of the mixed formulation models and the effectiveness of the computational procedure, which combines both the geometrically nonlinear terms and the contact conditions in one iteration loop.

## Introduction

Numerical modeling of the response characteristics of aircraft tires remains one of the most challenging applications of computational structural mechanics. There are several aspects of this problem that can lead to numerical difficulties and/or excessive computational expense. During normal aircraft operations, these tires are subjected to large displacements and temperature gradients. The tire is a composite structure composed of rubber, textile, and steel constituents that exhibits anisotropic and nonhomogeneous material properties. Furthermore, all the forces exerted on the tire associated with take-off and landing operations are generated through the tire-pavement interface; thus, any practical modeling tool must include a good contact algorithm. These facts and attendant difficulties emphasize the need to develop modeling strategies and analysis methods, including efficient contact algorithms, that are both powerful and economical. In recent years nonlinear analyses of static and dynamic problems involving contact have been the focus of intense research activities. Novel techniques that have emerged from these efforts include semianalytic finite-element models for nonlinear analysis of shells of revolution (refs. 1 and 2), reduced methods (refs. 3 and 4), and operator splitting techniques (refs. 5-7). Applications of these

new techniques to tire modeling are summarized in references 4, 7, and 8.

## Scope of Investigation

Current research in tire modeling and analysis at NASA Langley Research Center is aimed at developing an accurate and efficient strategy for predicting aircraft tire response. The focus of this paper is directed toward the developments in tire contact techniques. These contact algorithms are incorporated into a mixed formulation, two-field, two-dimensional finite-element code based on the moderate-rotation Sanders-Budiansky shell theory with the effects of transverse-shear deformation and laminated anisotropic material response included (refs. 9 and 10). The contact algorithm is based on the perturbed Lagrangian formulation (refs. 11 and 12) and utilizes the preconditioned conjugate gradient (PCG) iteration procedure (refs. 13-15) to determine contact area and pressure distribution. To demonstrate the capabilities of the analysis techniques, numerical studies are presented for an inflated Space Shuttle nose-gear tire statically loaded on a flat surface. The analysis assumes frictionless contact. Analytical results are compared with experimental measurements.

## Notation

$b_1, b_2$	parameters defining geometry of tire cross section (see fig. 3)
$c$	number of nodal points in contact in the element
$c_{ij}, d_{ij}, f_{ij}$	shell stiffness coefficients ( $i, j = 1, 2, 6$ )
$c_{44}, c_{45}, c_{55}$	transverse-shear stiffness coefficients of the tire (see eq. (A10))
$\vec{e}_s, \vec{e}_\theta$	tangential unit vectors in the meridional and circumferential directions
$E_{T_o}$	elastic modulus (see fig. 6)
$[F]$	flexibility matrix for an individual element
$F_c$	contact force
$\{\tilde{f}(Z, p)\}$	vector defined in equations (7)
$\{G(X)\}$	vector of nonlinear terms (see eq. (3))
$\{\bar{G}(X)\}$	vector of nonlinear terms in equations (4) and (5)
$\{\tilde{G}(Z)\}$	vector of nonlinear contributions to the global equations

$\bar{g}$	current gap (measured in the direction of the normal to the contact surface)	$R_1, R_2$	principal radii of curvature in meridional and circumferential directions
$\bar{g}_o$	initial gap	$r$	normal distance from tire axis to the reference surface
$\{g_o\}$	vector of initial gaps for contact element	$r_o$	$= r$ at $\xi = 0$
$\{H\}$	vector of stress-resultant parameters	$[S]$	strain-displacement matrix for an individual element
$h$	total thickness of tire	$s$	meridional coordinate of tire (see fig. 1)
$\bar{h}$	nondimensional thickness of tire (see fig. 4)	$[T]$	transformation matrix
$h_k$	thickness of individual layers of two-dimensional shell model	$T_n$	intensity of contact pressure (acting normal to contact surface)
$h_o$	total thickness of tire at $\xi = 0$ (see fig. 3)	$U$	strain energy density (strain energy per unit area)
$[\tilde{K}]$	global linear stiffness matrix	$u, v, w$	displacement components of the reference surface of the tire in the meridional, circumferential, and normal directions (see fig. 1)
$M_s, M_\theta, M_{s\theta}$	bending and twisting stress resultants (see fig. 1)		normal displacement at $\xi = \theta = 0$ (see fig. 9)
$\{M(H, X)\}$	vector of nonlinear terms (see eq. (3))	$\{\bar{X}\}$	vector of nodal displacements in the shell coordinate system
$m$	number of displacement nodes in the element	$\{\bar{X}\}$	vector of nodal displacements in Cartesian coordinate system
$N$	shape functions used for approximating generalized displacements and Lagrange multipliers	$x, y, z$	Cartesian coordinate system
$N_s, N_\theta, N_{s\theta}$	extensional stress resultants	$x_3$	coordinate normal to tire reference surface (see fig. 1)
$n$	total number of degrees of freedom	$\{Z\}$	global response vector
$\{P\}$	normalized external load parameter	$\varepsilon$	penalty parameter
$\{\tilde{P}\}$	global vector of normalized external loads and initial gaps	$\varepsilon_s, \varepsilon_\theta, 2\varepsilon_{s\theta}$	extensional strains of reference surface of tire
$P_n$	nodal (contact) force normal to contact surface	$2\varepsilon_{s3}, 2\varepsilon_{\theta 3}$	transverse-shear strains of tire
$p$	load parameter	$\theta$	circumferential (hoop) coordinate of tire (see fig. 1)
$p_o$	intensity of inflation pressure	$\tilde{\theta}$	orientation angle used in equation (13) and table 5
$p_s, p_\theta, p$	intensity of external loading in coordinate directions (see fig. 1)	$\theta_k$	orientation angle of tire cord, deg
$[Q], [R]$	elemental matrices associated with the contact condition and the regularization term in the functional	$\kappa_s, \kappa_\theta, 2\kappa_{s\theta}$	bending strains of tire
$Q_s, Q_\theta$	transverse-shear stress resultants (see fig. 1)	$\kappa_1, \kappa_2$	principal curvatures in meridional and circumferential directions of reference surface of shell model
$q$	load parameter	$\kappa_{1,o}, \kappa_{2,o}$	principal curvatures at $\xi = 0$

$\lambda$	Lagrange multiplier, representing intensity of contact pressure acting normal to contact surface
$\{\lambda\}$	vector of nodal values of Lagrange multipliers
$\xi$	dimensionless coordinate along meridian (see fig. 4)
$\Pi$	functional
$\phi$	rotation about the normal to tire reference surface
$\phi_s, \phi_\theta$	rotational components of reference surface of tire (see fig. 1)
$\Omega^{(e)}$	element domain
$\Omega_c$	contact surface
$\partial_s$	$\equiv \partial/\partial s$
$\partial_\theta$	$\equiv \partial/\partial\theta$
Superscripts:	
(e)	individual elements
$i, j$	indices of shape functions for approximating Lagrange multipliers
$i'$	index of shape function for approximating generalized displacements ( $i' = 1, m$ )
$r$	number of iteration cycles
$t$	matrix transposition
Subscript:	
conv	converged solution

## Mathematical Formulation

The analytical formulation for frictionless contact of aircraft tires is based on a form of the moderate-rotation, Sanders-Budiansky shell theory with the effects of large displacements and transverse-shear deformation included. A mixed formulation is used in which the fundamental unknowns consist of five generalized displacements and eight stress resultants. The sign convention for the generalized displacements and stress resultants is given in figure 1. The fundamental equations of the shell theory used herein are given in references 9 and 10 and are summarized in appendix A.

### Contact Condition

Figure 2 shows the characteristics of frictionless contact of a shell pressed against a rigid plate:  $\Omega_c$

refers to the contact region;  $\bar{g}_o$  is the initial gap between the shell and the plate;  $\bar{g}$  is the current gap (both  $\bar{g}_o$  and  $\bar{g}$  are measured normal to  $\Omega_c$ ), and  $T_n$  is the normal traction on  $\Omega_c$ . The contact condition can be expressed by the following inequalities and equation, which must be satisfied at each point on the contact surface  $\Omega_c$ :

$$\bar{g} \geq 0 \quad (1a)$$

$$T_n \leq 0 \quad (1b)$$

$$T_n \bar{g} = 0 \quad (1c)$$

The first inequality (eq. (1a)) represents the kinematic condition of no penetration of the rigid plate (zero gap for the contact points). The second inequality (eq. (1b)) is the static condition of compressive (or zero) normal tractions. The third equation (eq. (1c)) states that there is zero work done by the contact stresses (i.e., the contact stresses exist at the points where the tire is in contact with the rigid plate). The following inequalities are henceforth referred to as the *inactive contact conditions*:

$$\bar{g} > 0 \quad (1d)$$

$$T_n > 0 \quad (1e)$$

## Governing Finite-Element Equations

The discrete equations governing the response of the tire are obtained by applying a modified form of the two-field Hellinger-Reissner mixed variational principle. The modification consists of augmenting the functional of that principle by two terms: the Lagrange multiplier associated with the nodal contact pressures and a regularization term which is quadratic in the Lagrange multipliers. For detailed discussion of the perturbed and the augmented Lagrangian formulations, see references 11, 12, and 16.

The modified functional has the following form:

$$\Pi = \Pi_{HR} + \int_{\Omega_c} \left[ \bar{\lambda} \bar{g} - \frac{1}{2\varepsilon} (\bar{\lambda})^2 \right] d\Omega \quad (2)$$

where  $\Pi_{HR}$  is the functional of the Hellinger-Reissner variational principle,  $\bar{\lambda}$  is the Lagrange multiplier, and  $\varepsilon$  is the penalty parameter associated with the regularization term. The explicit forms of  $\Pi_{HR}$  for axisymmetric shells are given in reference 4. Note that the addition of the regularization term amounts to approximating the rigid plate by continuously distributed springs with stiffness  $\varepsilon$ , for sufficiently large  $\varepsilon$ . As  $1/\varepsilon$  approaches zero, the continuous springs become the rigid plate.

The shape functions used in approximating the generalized displacements and the Lagrange multipliers are selected to be the same and differ from those used in approximating the stress resultants. Moreover, because of the nature of the functional  $\Pi$  in equation (2), the continuity of neither the stress resultants nor the Lagrange multiplier is imposed at the interelement boundaries.

The finite-element equations for each individual element can be cast in the following compact form:

$$\begin{bmatrix} -F & S & \cdot \\ S^t & \cdot & Q \\ \cdot & Q^t & \frac{R}{\varepsilon} \end{bmatrix}^{(e)} \begin{Bmatrix} H \\ X \\ \lambda \end{Bmatrix} + \begin{Bmatrix} G(X) \\ M(H, X) \\ \cdot \end{Bmatrix}^{(e)} - \begin{Bmatrix} \cdot \\ pP \\ g_o \end{Bmatrix} = 0 \quad (3)$$

where  $\{H\}$ ,  $\{X\}$ , and  $\{\lambda\}$  are the vectors of the stress-resultant parameters, nodal values of the generalized displacements, and the nodal values of the Lagrange multipliers, respectively;  $[F]$  is the matrix of linear flexibility coefficients;  $[S]$  is the strain-displacement matrix;  $[Q]$  and  $[R]$  are the matrices associated with the contact condition and the regularization term in the functional (see appendix B);  $\{G(X)\}$  and  $\{M(H, X)\}$  are vectors of nonlinear terms;  $\{g_o\}$  is the vector of initial gaps in the contact region  $\Omega_c$ . A dot refers to a zero submatrix or subvector; superscript  $(e)$  refers to individual elements;  $\{P\}$  is the normalized external load vector;  $p$  is a load parameter. As the load is incremented, only the value of the load parameter  $p$  changes, and the normalized load vector  $\{P\}$  is constant. The formulas for the elemental arrays  $[F]$ ,  $[S]$ ,  $\{G(X)\}$ ,  $\{M(H, X)\}$ , and  $\{P\}$  are given in reference 7. The formulas for the elemental arrays  $[Q]$  and  $[R]$  are given in appendix B.

Note that the size of the coefficient matrices  $[R]$ ,  $[Q]$ , and  $\{g_o\}$  varies with the number of active contact conditions. The difficulty associated with an equation system whose size varies during the solution process was alleviated by allowing the Lagrange multipliers to be discontinuous at interelement boundaries and then eliminating them on the element level. If the stress-resultant parameters and Lagrange multiplier parameters are eliminated from equation (3), then the following equations in terms of nodal displacements  $\{X\}$  are obtained:

$$\begin{aligned} & \left[ [S]^t [F]^{-1} [S] - \varepsilon [Q][R]^{-1}[Q]^t \right]^{(e)} \{X\}^{(e)} \\ & + \{\bar{G}(X)\}^{(e)} + \varepsilon [Q][R]^{-1}\{g_o\}^{(e)} - p\{P\}^{(e)} = 0 \end{aligned} \quad (4)$$

where

$$\{\bar{G}(X)\}^{(e)} = [S]^t [F]^{-1} \{G(X)\}^{(e)} + \{M(H, X)\}^{(e)} \quad (5)$$

and the vector  $\{H\}$  in  $\{M(H, X)\}$  is replaced by its expression in terms of  $\{X\}$ .

To simplify the treatment of the contact conditions, the displacement components are transformed from shell coordinates  $(s, \theta, x_3)$  to the global Cartesian coordinates  $(x, y, z)$  before assembly. The relations between the displacement vector in the shell coordinates,  $\{X\}^{(e)}$ , and the corresponding vector in Cartesian coordinates,  $\{\bar{X}\}^{(e)}$ , can be written in the following compact form:

$$\{X\}^{(e)} = [T]\{\bar{X}\}^{(e)} \quad (6)$$

where  $[T]$  is the transformation matrix. The different arrays in the finite-element equations are transformed accordingly. The explicit form of the transformation relations is given in appendix C.

### Solution of Nonlinear Algebraic Equations

Discrete equations governing the response of the tire are obtained by assembling the elemental contributions in equations (3) or (4) and can be written in the following form:

$$\{\tilde{f}(Z, p)\} = [\tilde{K}]\{Z\} + \{\tilde{G}(Z)\} - p\{\tilde{P}\} = 0 \quad (7)$$

where  $[\tilde{K}]$  is the global linear stiffness matrix of the tire;  $\{\tilde{G}(Z)\}$  is the vector of nonlinear contributions;  $\{\tilde{P}\}$  is the global vector of normalized external loads and initial gaps; and  $\{Z\}$  is the global response vector of the tire obtained by assembling the contributions from the subvectors  $\{H\}$ ,  $\{X\}$ , and  $\{\lambda\}$ .

The nonlinear algebraic equations (eqs. (7)) are solved and the contact region and the contact pressures are determined by using an incremental-iterative technique (i.e., a predictor-corrector computation method) in which the response vector  $\{Z\}$  corresponding to a particular value of the load parameter  $p$  is used to calculate a suitable approximation (predictor) for  $\{Z\}$  at a different value of  $p$ . This approximation is then chosen as an initial estimate for  $\{Z\}$  in a corrective iterative scheme such as the Newton-Raphson technique. In each Newton-Raphson iteration the contact conditions are checked and updated.

## Computational Procedure To Determine Contact Pressures

The computational procedure used to determine the contact region and the contact pressures is outlined in this section. Nonlinearities due to large displacements (moderate rotations) and the contact condition are combined into a single iteration loop. Reference 15 advocates a two-level (nested) iteration scheme. For the two-level scheme, the inner iteration loop accounts for the contact conditions associated with the contact pressures, and the outer iteration loop uses the Newton-Raphson iteration scheme. Numerical experiments have demonstrated that for frictionless contact problems the two-level iterative scheme requires more iterations than the single-level scheme (see ref. 17).

The solution of the governing discrete equations of the entire structure generates the nodal displacements, the stress-resultant parameters, and the values of the Lagrange multipliers at the contact nodes. For each individual element in contact, the intensity of the contact pressure at a node,  $T_n$ , is equal to the value of the Lagrange multiplier  $\bar{\lambda}$  at the same node. The contact pressures are also related to the nodal forces normal to the contact surface,  $P_n^i$ , as follows:

$$P_n^i = \int_{\Omega^{(e)}} N^i N^j d\Omega T_n^j \quad (8)$$

where  $N^i$  are the shape functions used in approximating the Lagrange multiplier and the generalized displacements, and  $\Omega^{(e)}$  is the domain of the contact element. The range of both  $i$  and  $j$  in equation (8) is from 1 to the number of displacement nodes in the element. Other approaches for determining the contact pressures are discussed in reference 18.

The computational procedure used in the present study is summarized as follows:

### Preprocessing and Initial Calculation Phases

- Step 1. Model tire geometry, evaluate stiffness coefficients (ref. 19), and generate input data including transformation matrices.
- Step 2. Select estimates for the penalty parameter and assume the contact status at the selected contact nodes.
- Step 3. Generate linear element arrays.

### Solution Phase

- Step 4. Solve inflation pressure case without contact using Newton-Raphson iteration scheme.

- Step 5. Generate initial gap between the inflated tire configuration and the flat plate at designated contact nodes.
- \* Begin displacement incrementation loop.
- \* Begin combined contact and Newton-Raphson iteration loop.
- Step 6. Generate nonlinear element arrays, eliminate the stress resultants and the Lagrange multipliers from the elemental equations, and assemble the left- and right-hand sides of the equations.
- Step 7. Solve equations (7) for the incremental displacements.
- Step 8. Update the response vector for displacements, stress resultants, and the Lagrange multipliers:

$$\{Z^{(r+1)}\} = \{Z^{(r)}\} + \{\Delta Z^{(r)}\} \quad (9)$$

- Step 9. Check the contact status and modify the contact conditions at each node as needed:

If  $\bar{g} > 0$ , and  $\bar{\lambda} > 0$ , then the contact constraint is inactive

If  $\bar{g} < 0$ , then the constraint is active

If the contact constraint is the same as that previously assumed, then continue. Otherwise, add the active contact contribution to the list of nodes with active constraints or subtract the contact contribution from that list if the constraint is now inactive and return to step 6.

- Step 10. Check convergence of the Newton-Raphson iterations:

$$e = \frac{[\{\Delta Z\}^t \{\Delta Z\} / \{Z\}^t \{Z\}]^{1/2}}{n} < \text{Tolerance} \quad (10)$$

where  $e$  is the solution error,  $n$  is the total number of degrees of freedom in the model, and the tolerance is prescribed. If convergence is achieved, then compute the contact forces at each contact node by

$$P_n^i = \int_{\Omega^{(e)}} N^i \bar{\lambda} d\Omega \quad (11)$$

and continue. Otherwise return to step 6.

- Step 11. If the prescribed displacement is greater than the specified maximum displacement, then stop. Otherwise, add additional displacement and return to step 6.

The mixed-formulation finite elements used in this study have nine displacement nodes and four

stress-resultant nodes and are designated as M9-4 elements in table 1.

## Comments on Mixed Models, Perturbed Lagrangian Formulation, and Computational Procedure

The following comments regarding the mixed models, the perturbed Lagrangian formulation, and the computational procedure used herein are in order:

1. The nonlinear terms in the finite-element equations of the mixed model (eqs. (3)) have a simpler form than those of the corresponding displacement model (eq. (5)).
  2. Equations (3) include both the Lagrange multiplier approach and the penalty method as special cases, as follows:
    - a. As the penalty parameter  $\varepsilon$  approaches infinity, equations (3) reduce to those of the Lagrange multiplier approach.
    - b. When the Lagrange multiplier terms are eliminated in equations (3), the resulting equations are identical to the penalty method.
  3. The perturbed Lagrangian formulation alleviates two of the drawbacks associated with the Lagrange multiplier approach and the penalty method, namely:
    - a. The regularization term in the functional results in replacing one of the zero diagonal blocks in the discrete equations of the Lagrange multiplier approach by the diagonal matrix  $[R]/\varepsilon$  in equations (3).
    - b. The contact condition is satisfied exactly by transforming the constrained problem to an unconstrained problem through the introduction of Lagrange multipliers (the term  $\int_{\Omega_c} \bar{\lambda} \bar{g} d\Omega$  in eq. (2)) results in replacing the contact condition by the perturbed condition:
- $$\frac{1}{\varepsilon} [R] \{ \lambda \} + [Q]^t \{ X \} - \{ g_o \} = 0 \quad (12)$$
4. An important consideration in the perturbed Lagrangian formulation and in any penalty formulation is the proper selection of the penalty parameter  $\varepsilon$ . With the foregoing mixed models, the penalty parameter can be chosen independently of the element size without adversely affecting the performance of the model. The accuracy of the

solution increases with increasing values of the penalty parameter. However, for very large values of  $\varepsilon$ , the equations become ill-conditioned and thus round-off errors increase.

5. The elemental arrays  $[F]$ ,  $[S]$ ,  $\{G(X)\}$ ,  $\{M(H, X)\}$ , and  $\{P\}$  are evaluated numerically using a Gauss-Legendre formula. The arrays  $[Q]$ ,  $[R]$ , and  $\{g_o\}$  are evaluated using a Newton-Cotes formula. In both cases the number of quadrature points used is the same as the number of displacement nodes in the element. This results in under-integrating the arrays  $[Q]$  and  $[R]$  and avoids the oscillatory behavior of the contact pressures that has been observed when the arrays are fully integrated. Note that the use of Newton-Cotes formula allows the contact pressures to be evaluated at the displacement nodes.

## Results and Discussion

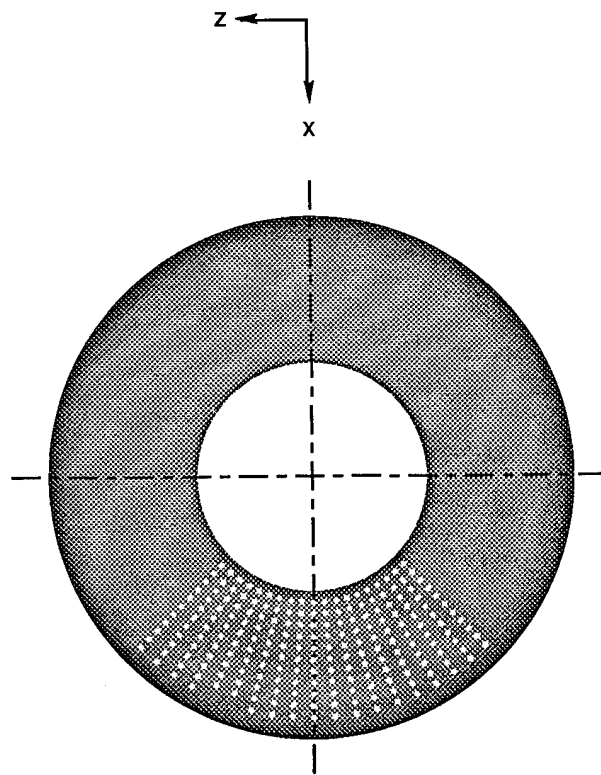
Numerical studies were performed to assess the accuracy of the two-dimensional shell tire model, the effectiveness of the proposed computational procedure, and the performance of the contact algorithm. To conduct these studies the  $32 \times 8.8$ , type VII, 16-ply rating, Space Shuttle orbiter nose-gear tire was modeled as a two-dimensional, laminated shell with variable thickness and variable stiffness characteristics. The outer surface of the tire was taken to be the reference surface of the shell model. The geometric characteristics of the tire are given in figure 3. The tire carcass is constructed of 10 lamina of nylon and rubber with an additional reinforcing ply beneath the tire tread as shown in figure 4. The tire has a three-groove tread pattern, but in this investigation the tire model assumes a smooth tread pattern instead. The rated load for the tire is 15 000 lb at an inflation pressure of 320 psi. All experiments were conducted at an inflation pressure of 300 psi. The following sections describe the experimental measurements used to establish the tire geometry and to define the global elastic response of the tire to inflation and static vertical loading conditions. These sections also present an evaluation of the tire stiffness characteristics and numerical results with some limited comparisons between the analytical predictions and the experimental measurements.

### Modeling of Tire Geometry

A Space Shuttle nose-gear tire was cut into sections and used to obtain accurate measurements of the cross-sectional profile of the uninflated tire. A smoothed spline under tension was used to fit a curve through the measured coordinates of the cross-sectional profile in a least-squares sense (see refs. 20

and 21). Because of symmetry, only half the cross section was modeled. A smooth variation of the second derivative,  $\frac{d^2x}{dz^2}$ , was achieved by adjusting the standard deviations of the measured profile at the data points. For a detailed description of spline smoothing techniques, see references 21 to 23.

The spline function with the tension function factor set equal to 0.1 and slope continuity enforced at both ends of the curves was used to generate additional points along the meridian of the tire. The interpolation procedure is outlined in reference 20, and the resulting geometric characteristics of the tire are presented in figure 5. The thickness of the tire carcass at the nodal points of the finite-element model was computed along the normal vector to the tire reference (outer) surface by locating the points of intersection of the normal vectors with the inner surface of the tire carcass. To facilitate these computations the tire inner surface was approximated by a set of third-degree polynomials.



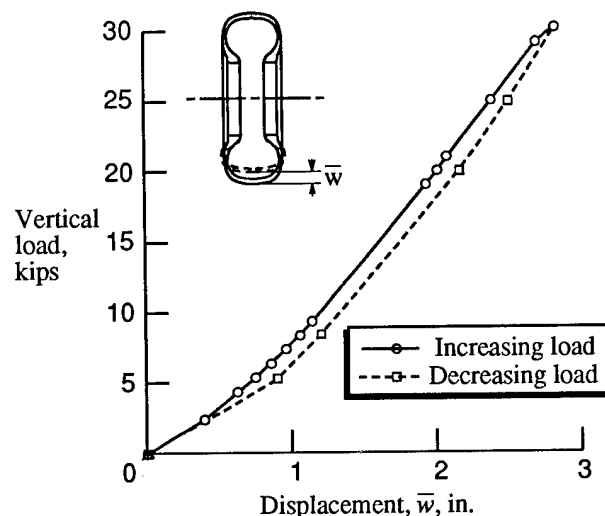
Sketch 1. Arrangement of photogrammetry targets on Space Shuttle nose-gear tire.

#### Measurements of Inflated Cross-Sectional Profile and Vertical Load-Deflection Response

Close-range photogrammetry techniques were used to define the inflated profile of the Space Shuttle

orbiter nose-gear tire. To facilitate these measurements, 209 circular, reflective targets were attached to the tire as shown in sketch 1. The targets were aligned along 19 meridional lines of the tire sidewall and a video camera was used to record the target positions from 10 camera locations. A stereo photography triangulation technique (refs. 24 and 25) was used to define the location of each target in a global coordinate system from these video images. The rms measurement accuracies were found to be 1.3 mils, 2.9 mils, and 1.5 mils in the  $x$ -,  $y$ -, and  $z$ -coordinate directions, respectively.

Static vertical load-deflection tests were conducted on the inflated Space Shuttle nose-gear tire to obtain a global measure of the tire elastic response. For these tests the tire was slowly lowered onto a flat plate until a maximum vertical load of approximately 30 000 lb was obtained and then slowly unloaded until the tire lost contact with the surface. During this loading process, an  $x-y$  plotter was used to monitor the resulting tire hysteresis loop as shown in sketch 2.



Sketch 2. Static vertical load-deflection curve for Space Shuttle nose-gear tire.

#### Evaluation of Stiffness Coefficients of Two-Dimensional Shell Model

The cord-rubber composite was treated as a laminated material. For the purpose of computing stiffness variations in the meridional direction, the tire model was divided into seven regions, as shown in figure 4. Thickness of the individual carcass plies was measured at the interfaces between the regions and these values are given in table 2. A linear variation was assumed for the thickness within each region. The thickness of the tire tread and sidewall covering was computed by subtracting the sum of the

individual ply thicknesses from the total thickness of the carcass at each location.

The material properties of the different plies were obtained with the mechanics of material approach, which has been widely applied to rigid composites. (See refs. 26 and 27.) The elastic constants of the tire constituents used in this study are presented in table 3. It was assumed that nylon cords of two different diameters were used in the construction of the tire: 0.022 in. for the bottom two plies and the tread reinforcement in region I, and 0.031 in. for all other plies.

The cord end counts (epi) for individual plies at the region interfaces are given in table 4. A linear variation was assumed for epi within each region. The formulas for evaluating the composite elastic coefficients for each ply, from the properties of the ply constituents, are given in reference 19.

The stress-strain relationships of the two-dimensional shell were obtained by first transforming the stiffness of each of the individual layers to the global shell coordinates ( $s$  and  $\theta$ ) and then integrating these coefficients through the thickness. The cord orientations in the individual plies of each region are given in table 5. The following formula was used to determine  $\theta_k$ , the angle (in degrees) measured from the  $s$ -axis to the  $\theta$ -axis, at the numerical quadrature points:

$$\tilde{\theta} = \text{Max} \left\{ (54.382 - 3.884\xi - 148.96\xi^2)^\circ, 33^\circ \right\} \quad (13)$$

where  $\xi$  is the dimensionless coordinate along the tire meridian. The resulting shell constitutive relations are given in appendix A. The meridional variations of the stiffness coefficients are shown in figure 6.

### **Analysis of Space Shuttle Nose-Gear Tire Under Inflation Pressure Loading**

To access the accuracy of the two-dimensional shell model of the Space Shuttle nose-gear tire, the deformations produced by uniform inflation pressure of 300 psi, acting normal to the interior surface, were calculated using the geometrically nonlinear shell theory. A strip of 30 finite elements was used in modeling the tire cross section (a total of 480 stress-resultant parameters and 293 nonzero generalized displacement parameters). The measured and predicted cross-sectional profiles for the Space Shuttle nose-gear tire are presented in figure 7. The primary effect of inflation pressure is to expand the tire profile in the cross-sectional regions I to V. The predicted inflated profile is in excellent agreement with

the measured profiles. Additional information on inflation pressure results is presented in reference 19.

### **Analysis of Inflated Space Shuttle Nose-Gear Tire in Contact With a Flat Plate**

Three different models were used in the analysis of the Space Shuttle nose-gear tire in contact with a flat plate. These models denoted as model 1, model 2, and model 3 are depicted in figure 8. Each model employed 360 elements in the region outside the contact zone ( $\theta < -0.2\pi$ ,  $\theta > 0.2\pi$ ). Model 1 included 180 elements in the contact region of the tire ( $-0.2\pi \leq \theta \leq 0.2\pi$ ) for a total of 540 elements. Model 2 used a refined mesh within the contact region with 360 contact elements for a total of 720 elements, and model 3 employed a more refined mesh in the contact zone with 720 contact elements for a total of 1080 elements. These models were used to study the convergence characteristics of the frictionless tire contact problem.

The load-deflection characteristics of the inflated Space Shuttle nose-gear tire subjected to static vertical loading against a rigid, flat plate are shown in figure 9. The faired load-deflection experimental data for the tire during the loading cycle are denoted by the solid line in the figure. These results indicate that the global response of the tire to this loading condition is that of a stiffening spring. The unloading data shown in sketch 2 are not reproduced in this figure because the tire models presented herein do not account for damping effects. Predicted load-deflection responses from model 1 are denoted by plus signs and results from model 3 are denoted by triangular symbols. The analytical results from both models are in excellent agreement with the experimental data. This result suggests that the global response of the tire to contact loads will not be strongly influenced by the inclusion of friction in the contact algorithm. Furthermore, the close agreement between the two analytical models suggests that the global response of the tire is adequately represented by the coarse-mesh model 1.

Predicted deformed configurations of the inflated Space Shuttle nose-gear tire subjected to contact loading at increasing vertical loads are shown in figure 10. The graphic results show a sequence of deformed configurations for the tire as the applied deflection is increased from initial contact at no load through a vertical deflection of 1.80 in. with a load of approximately 24 000 lb. The top two rows of pictures show the deformation sequence from the three-quarter side and three-quarter front views and the bottom two rows show the same deformation

sequence from the full side and front views. These results were generated from model 3 output.

Predicted growth in tire contact area is presented in figure 11. The three views show the extent of contact predicted by model 3 for tire deflections of 0.90 in., 1.5 in., and 1.80 in. and vertical loads of approximately 7000 lb, 13000 lb, and 24000 lb, respectively.

Predicted variations in contact pressure distribution for the Space Shuttle nose-gear tire are shown in figure 12. Analytical results are presented as color contour plots to show the predicted distribution of tire footprint pressures from model 3 for tire deflections ranging from 0.90 in. to 1.80 in. Peak contact pressures are predicted to occur in the periphery of the contact zone. For the Space Shuttle nose-gear tire inflated to 300 psi the peak contact pressure is approximately 350 psi. The effect of increasing tire deflection, and hence vertical load, is to distribute these peak pressures over a larger area; however, the magnitude of the peak contact pressure for the 0.90-in. deflection case is equivalent to the peak contact pressure for the 1.80-in. deflection case.

Convergence characteristics of contact pressure distribution are shown in figure 13. To illustrate convergence characteristics of the predicted contact pressure distribution, contact pressures along the tire meridian at the center of contact (section a-a), circumferentially along the tire equator (section b-b), and circumferentially along the edge of contact (section c-c) are presented in the figure. The coarse-mesh model 1 is shown to predict higher peak contact pressures in the periphery of contact than the two refined-mesh models along the central tire meridian and along the tire equator. Along the circumferential edge of contact, the model with the most refined mesh was needed to obtain a converged solution.

One means of showing regions of high strain due to loads on a complex structure such as a tire is strain energy density. Calculated variations in the strain energy density distribution for the Space Shuttle nose-gear tire are shown in figure 14 in the form of color contour plots. Total strain energy density is presented in figure 14(a) and transverse-shear strain energy density is presented in figure 14(b). Total strain energy density is primarily influenced by the inflation pressure load. Since the normal tractions associated with contact are compressive, the total strain energy density is reduced in the region of contact. Total strain energy density is also reduced in the lower sidewall area near the bead. Transverse-shear strain energy density is maximized in the tire sidewall near the tire contact zone and along the

lower sidewall near the tire bead. In the contact region the transverse-shear strain energy represents about 25 percent of the total strain energy.

Analytical results presented in figures 11, 12, and 14 indicate that the response characteristics of the tire exhibit inversion (polar) symmetry with respect to the coordinate center. As indicated in reference 7, this symmetry condition can be exploited to reduce the computational effort associated with tire modeling.

The influence of the magnitude of the penalty parameter on the accuracy of the total strain energy and the total contact force is presented in figure 15. The strain energy ratio, denoted by the dashed line, and the contact force ratio, denoted by the solid line, are plotted as a function of the base 10 logarithm of the penalty parameter in the figure. Results in the figure indicate that total calculated strain energy and total contact force are insensitive to variations in the penalty parameter over the range of  $10^6$  to  $10^{15}$ .

### Concluding Remarks

A computational procedure is presented for the solution of frictionless contact problems of aircraft tires. The Space Shuttle nose-gear tire is modeled using a two-dimensional laminated anisotropic shell theory with the effects of variation in material and geometric parameters, transverse-shear deformation, and geometric nonlinearities included. The contact conditions are incorporated into the formulation by using a perturbed Lagrangian approach with the fundamental unknowns consisting of the stress resultants, the generalized displacements, and the Lagrange multipliers associated with the contact conditions. The elemental arrays are obtained by using a modified two-field, mixed variational principle. The modification consists of augmenting the functional of that principle by two terms: the Lagrange multiplier vector associated with nodal contact pressures and a regularization term which is quadratic in the Lagrange multiplier vector.

The shape functions used in approximating the generalized displacements and the Lagrange multipliers are selected to be the same and differ from those used to approximate the stress resultants. The stress resultants and the Lagrange multipliers are allowed to be discontinuous at the interelement boundaries. The nonlinearities due to both large displacements, moderate rotations, and the contact conditions are combined into the same iteration loop and are handled by using the Newton-Raphson iterative scheme.

Numerical results are presented for the Space Shuttle nose-gear tire subjected to inflation

pressure and contact loads against a rigid flat plate. The measured and computed inflated profiles of the tire are in excellent agreement, and the measured and calculated load deflection curves of the tire for static vertical loading against a flat plate are also in excellent agreement. The numerical studies have demonstrated the high accuracy of the mixed mod-

els and the effectiveness of the computational procedure, which combines both the geometrically nonlinear terms and the contact conditions in one iteration loop.

NASA Langley Research Center  
Hampton, VA 23665-5225  
February 27, 1991

## Appendix A

### Fundamental Equations of Shell Theory Used in Present Study

The fundamental equations of the Sanders-Budiansky type shell of revolution used in the present study are summarized herein. The effects of laminated, anisotropic material response and transverse-shear deformation are included.

#### Strain-Displacement Relationships

$$\varepsilon_s = \partial_s u + \frac{w}{R_1} + \frac{1}{2} \left( \frac{u}{R_1} - \partial_s w \right)^2 + \frac{1}{2} \phi^2 \quad (A1)$$

$$\varepsilon_\theta = \frac{\partial_s r}{r} u + \frac{1}{r} \partial_\theta v + \frac{w}{R_2} + \frac{1}{2} \left( \frac{v}{R_2} - \frac{1}{r} \partial_\theta w \right)^2 + \frac{1}{2} \phi^2 \quad (A2)$$

$$2\varepsilon_{s\theta} = \frac{1}{r} \partial_\theta u + \left( \partial_s - \frac{\partial_s r}{r} \right) v + \left( \frac{u}{R_1} - \partial_s w \right) \left( \frac{v}{R_2} - \frac{1}{r} \partial_\theta w \right) \quad (A3)$$

$$\kappa_s = \partial_s \phi_s \quad (A4)$$

$$\kappa_\theta = \frac{\partial_s r}{r} \phi_s + \frac{1}{r} \partial_\theta \phi_\theta \quad (A5)$$

$$2\kappa_{s\theta} = \frac{1}{r} \partial_\theta \phi_s + \left( \partial_s - \frac{\partial_s r}{r} \right) \phi_\theta + \left( \frac{1}{R_2} - \frac{1}{R_1} \right) \phi \quad (A6)$$

$$2\varepsilon_{s3} = -\frac{u}{R_1} + \partial_s w + \phi_s \quad (A7)$$

$$2\varepsilon_{\theta3} = -\frac{v}{R_2} + \frac{1}{r} \partial_\theta w + \phi_\theta \quad (A8)$$

where  $\varepsilon_s$  and  $\varepsilon_\theta$  are the extensional strains in the meridional and circumferential directions;  $2\varepsilon_{s\theta}$  is the extensional shear strain;  $\kappa_s$  and  $\kappa_\theta$  are the bending strains in the meridional and circumferential directions;  $2\kappa_{s\theta}$  is the twisting strain;  $2\varepsilon_{s3}$  and  $2\varepsilon_{\theta3}$  are the transverse-shear strains;  $\partial_s \equiv \partial/\partial s$ ;  $\partial_\theta \equiv \partial/\partial\theta$ ; and  $\phi$  is the rotation around the normal to the shell, which is given by

$$\phi = \left[ -\frac{1}{r} \partial_\theta u + \left( \partial_s + \frac{\partial_s r}{r} \right) v \right] \quad (A9)$$

The nonlinear terms that account for moderate rotations are underlined with dashes in equations (A1) to (A3).

#### Constitutive Relations

The shell is assumed to be made of a laminated, anisotropic, linearly elastic material. Every point of the shell is assumed to possess a single plane of elastic symmetry parallel to the middle surface. The relationships between the stress resultants and the strain measures of the shell are given by

$$\left\{ \begin{array}{l} N_s \\ N_\theta \\ N_{s\theta} \\ M_s \\ M_\theta \\ M_{s\theta} \\ Q_s \\ Q_\theta \end{array} \right\} = \left[ \begin{array}{cccccc|cc} c_{11} & c_{12} & \textcircled{c_{16}} & f_{11} & f_{12} & \textcircled{f_{16}} & \cdot & \cdot \\ & c_{22} & \textcircled{c_{26}} & f_{12} & f_{22} & \textcircled{f_{26}} & \cdot & \cdot \\ & & c_{66} & \textcircled{f_{16}} & \textcircled{f_{26}} & f_{66} & \cdot & \cdot \\ & & & d_{11} & d_{12} & \textcircled{d_{16}} & \cdot & \cdot \\ & & & & d_{22} & \textcircled{d_{26}} & \cdot & \cdot \\ & & & & & d_{66} & \cdot & \cdot \\ & & & & & & c_{55} & \textcircled{c_{45}} \\ & & & & & & & c_{44} \end{array} \right] \left\{ \begin{array}{l} \varepsilon_s \\ \varepsilon_\theta \\ 2\varepsilon_{s\theta} \\ \kappa_s \\ \kappa_\theta \\ \kappa_{s\theta} \\ 2\varepsilon_{s3} \\ 2\varepsilon_{\theta3} \end{array} \right\} \quad (\text{A10})$$

Symmetric

where  $c_{ij}$ ,  $f_{ij}$ , and  $d_{ij}$  ( $i, j = 1, 2, 6$ ) are shell stiffness coefficients. The nonorthotropic (anisotropic) terms are circled, and dots indicate zero terms.

## Appendix B Formulas for Elemental Arrays $[Q]$ , $[R]$ , and $\{g_o\}$

The explicit forms of the elemental arrays  $[Q]$ ,  $[R]$ , and  $\{g_o\}$  are given in this appendix. For convenience, each array is partitioned into blocks according to contributions from displacement and contact nodes. The expressions of the typical partitions are given in table B1. In table B1,  $N^i$  and  $N^j$  are the shape functions for the Lagrange multipliers and generalized displacements,  $m$  is the number of displacement nodes in the element,  $c$  is the number of nodal points in contact within the element, and  $\Omega^{(e)}$  is the element domain. The range of the indices  $i$  and  $j$  is from 1 to  $c$ , and the range of the index  $i'$  is from 1 to  $m$ ;  $\langle \tilde{g} \rangle$  is the unit ramp (or singularity) function defined as follows:

$$\langle \tilde{g} \rangle^n = \begin{cases} \tilde{g}^n & (\tilde{g} > 0) \\ 0 & (\tilde{g} \leq 0) \end{cases} \quad (B1)$$

where  $\tilde{g} = -\tilde{g}$  and  $n = 0$  or 1.

Table B1. Explicit Form of Typical Partitions  
of the Arrays  $[Q]$ ,  $[R]$ , and  $\{g_o\}$

Array	Number of partitions or blocks	Formula for typical partition
$[Q]$	$m \times c$	$\int_{\Omega^{(e)}} N^{i'} N^j \langle \tilde{g} \rangle^0 d\Omega$
$[R]$	$c \times c$	$- \int_{\Omega^{(e)}} N^i N^j \langle \tilde{g} \rangle^0 d\Omega$
$\{g_o\}$	$c$	$\int_{\Omega^{(e)}} N^i \langle \tilde{g} \rangle d\Omega$

## Appendix C

### Transformation of Elemental Arrays From Shell Coordinates to Global Cartesian Coordinates

The transformation of the displacement components from the shell coordinates  $(s, \theta, x_3)$  to the global Cartesian coordinates  $(x, y, z)$  is expressed by the following equation:

$$\{X\}^{(e)} = [T]\{\bar{X}\}^{(e)} \quad (C1)$$

where  $[T]$  is a block-diagonal transformation whose submatrix at each node is given by

$$\begin{matrix} [T]^{(n)} \\ (5 \times 5) \end{matrix} = \begin{bmatrix} \vec{e}_s & \vec{e}_\theta & \vec{e}_s \times \vec{e}_\theta & \vec{0} & \vec{0} \\ & & & 1 & 0 \\ & & \leftarrow 0 & & \\ & & & 0 & 1 \end{bmatrix} \quad (C2)$$

$\vec{e}_s$  and  $\vec{e}_\theta$  are the tangential unit vectors in the  $s$ - and  $\theta$ -directions, respectively;  $\vec{0}$  is the null vector;  $\{X\}^{(e)}$  and  $\{\bar{X}\}^{(e)}$  are the generalized displacements in shell coordinates and global Cartesian coordinates, respectively. Note that the rotation components  $\phi_s$  and  $\phi_\theta$  are not transformed since the outer surface of the tire was chosen as the reference surface and, therefore,  $\phi_s$  and  $\phi_\theta$  do not appear in the contact conditions.

The elemental matrices  $[S]$  and  $\left[ \frac{\partial M}{\partial \bar{X}} \right]$  and the external load vector  $\{P\}$  are transformed from the shell coordinates to the global Cartesian coordinates as follows:

$$[S] \rightarrow [S][T] \quad (C3)$$

$$\left[ \frac{\partial M}{\partial \bar{X}} \right] \rightarrow [T]^t \left[ \frac{\partial M}{\partial X} \right] [T] \quad (C4)$$

$$\{P\} \rightarrow [T]^t \{P\} \quad (C5)$$

The nonlinear vectors  $\{G(X)\}$  and  $\{M(H, X)\}$  are evaluated with displacement vector  $\{X\}$  expressed in terms of  $\{\bar{X}\}$  at the end of each iteration cycle.

## References

1. Schaeffer, Harry G.; and Ball, Robert E.: Nonlinear Deflections of Asymmetrically Loaded Shells of Revolution. AIAA Paper No. 68-292, Apr. 1968.
2. Wunderlich, W.; Cramer, H.; and Obrecht, H.: Application of Ring Elements in the Nonlinear Analysis of Shells of Revolution Under Nonaxisymmetric Loading. *Comput. Methods Appl. Mech. & Eng.*, vol. 51, no. 1-3, Sept. 1985, pp. 259-275.
3. Noor, Ahmed K.: On Making Large Nonlinear Problems Small. *Comput. Methods Appl. Mech. & Eng.*, vol. 34, no. 1-3, Sept. 1982, pp. 955-985.
4. Noor, Ahmed K.; Andersen, Carl M.; and Tanner, John A.: *Mixed Models and Reduction Techniques for Large-Rotation, Nonlinear Analysis of Shells of Revolution With Application to Tires*. NASA TP-2343, 1984.
5. Noor, Ahmed K.: Reduction Method for the Non-Linear Analysis of Symmetric Anisotropic Panels. *Int. J. Numer. Methods Eng.*, vol. 23, 1986, pp. 1329-1341.
6. Noor, Ahmed K.; and Peters, Jeanne M.: Nonlinear Analysis of Anisotropic Panels. *AIAA J.*, vol. 24, no. 9, Sept. 1986, pp. 1545-1553.
7. Noor, Ahmed K.; Andersen, Carl M.; and Tanner, John A.: *Exploiting Symmetries in the Modeling and Analysis of Tires*. NASA TP-2649, 1987.
8. Noor, Ahmed K.; and Tanner, John A.: *Advances in Contact Algorithms and Their Application to Tires*. NASA TP-2781, 1988.
9. Sanders, J. Lyell, Jr.: Nonlinear Theories for Thin Shells. *Q. Appl. Math.*, vol. 21, no. 1, Apr. 1963, pp. 21-36.
10. Budiansky, Bernard: Notes on Nonlinear Shell Theory. *J. Appl. Mech.*, vol. 35, no. 2, June 1968, pp. 393-401.
11. Simo, Juan C.; Wriggers, Peter; and Taylor, Robert L.: A Perturbed Lagrangian Formulation for the Finite Element Solution of Contact Problems. *Comput. Methods Appl. Mech. & Eng.*, vol. 50, no. 2, Aug. 1985, pp. 163-180.
12. Stein, E.; Wagner, W.; and Wriggers, P.: Finite Element Postbuckling Analysis of Shells With Nonlinear Contact Constraints. *Finite Element Methods for Nonlinear Problems*, P. G. Bergan, K. J. Bathe, and W. Wunderlich, eds., Springer-Verlag, c.1986, pp. 719-744.
13. Concus, Paul; Golub, Gene H.; and O'Leary, Dianne P.: A Generalized Conjugate Gradient Method for the Numerical Solution of Elliptic Partial Differential Equations. *Sparse Matrix Computations*, James R. Bunch and Donald J. Rose, eds., Academic Press Inc., 1976, pp. 309-332.
14. Adams, Loyce: m-Step Preconditioned Conjugate Gradient Methods. *SIAM J. Sci. & Stat. Comput.*, vol. 6, no. 2, Apr. 1985, pp. 452-463.
15. Wriggers, Peter; and Nour-Omid, Bahram: *Solution Methods for Contact Problems*. Rep. No. UCB/SESM-84/09 (Contract N00014-76-C-0013), Dep. of Civil Engineering, Univ. of California, July 1984.
16. Wriggers, P.; Wagner, W.; and Stein, E.: Algorithms for Non-Linear Contact Constraints With Application to Stability Problems of Rods and Shells. *Comput. Mech.*, vol. 2, 1987, pp. 215-230.
17. Noor, Ahmed K.; and Kim, Kyun O.: Mixed Finite Element Formulation for Frictionless Contact Problems. *Finite Elem. Anal. & Design*, vol. 4, no. 4, 1989, pp. 315-332.
18. Torstenfelt, Bo: Finite Elements in Contact and Friction Applications. Linköping Studies in Science and Technology. Dissertations. No. 103, Div. of Solid Mechanics and Strength of Materials, Dep. of Mechanical Engineering, Linköping Univ. (Linköping, Sweden), 1983.
19. Kim, Kyun O.; Noor, Ahmed K.; and Tanner, John A.: *Modeling and Analysis of the Space Shuttle Nose-Gear Tire With Semianalytic Finite Elements*. NASA TP-2977, 1990.
20. *User's Manual—IMSL Math/Library, Version 1.1*. MALB-USM-PERFCT-EN8901-1.1, IMSL, Inc., Jan. 1989.
21. Cline, Alan Kaylor: *Fitpack—A Software Package for Curve and Surface Fitting Employing Splines Under Tension*. Pleasant Valley Software, c.1985.
22. De Boor, Carl: *A Practical Guide to Splines*. Springer-Verlag, c.1978.
23. Reinsch, Christian H.: Smoothing by Spline Functions. *Numer. Math.*, vol. 10, no. 3, 1967, pp. 177-183.
24. Karara, H. M., ed.: *Non-Topographic Photogrammetry*, Second ed. American Soc. for Photogrammetry and Remote Sensing, 1989.
25. Schroeder, Lyle C.; Adams, Richard C.; Bailey, M. C.; Belvin, W. Keith; Butler, David H.; and Campbell, Thomas G.: *Near-Field Testing of the 15-Meter Hoop-Column Antenna*. NASA TM-4073, 1989.
26. Walter, J. D.: Cord Reinforced Rubber. *Mechanics of Pneumatic Tires*, Samuel K. Clark, ed., U.S. Dep. of Transportation, 1981, pp. 123-202.
27. Jones, Robert M.: *Mechanics of Composite Materials*. McGraw-Hill Book Co., c.1975.

Table 1. Characteristics of Mixed Finite-Element Model  
Used in the Numerical Studies

Designation	Number of displacement nodes	Maximum number of Lagrange multipliers	Number of parameters per stress resultant	Number of quadrature points*
M9-4	$3 \times 3$	$3 \times 3$	$2 \times 2$	$3 \times 3$

\* All elemental arrays are evaluated using Gauss-Legendre quadrature formulas except for  $[Q]$ ,  $[R]$ , and  $\{g_o\}$ , which are evaluated using Newton-Cotes formulas.

Table 2. Variation of Ply Thickness  $h_k/h_o$

$[h_o = 0.7513 \text{ in.}]$

Ply number (top to bottom)	$h_k/h_o$ for region—						
	I	II	III	IV	V	VI	VII
1 (tread and sidewall)	$h_1 = h - \sum_{k=2}^{16} h_k$						
<sup>a</sup> 2	0.0865— .0865	0.0865— .0658	0.0658— .0692	0.0692— .0813	0.0801— .0937	0.0681— .1238	0.0918— .1240
3	0.0865— .0865	0.0865— .0658	0.0658— .0692	0.0692— .0813	0.0801— .0937	0.0681— .1238	0.0918— .1240
4	0.0865— .0865	0.0666— .0506	0.0506— .0532	0.0692— .0813	0.0488— .0571	0.0523— .0950	0.0652— .0880
5	0.0666— .0666	0.0666— .0506	0.0506— .0532	0.0426— .0500	0.0488— .0571	0.0523— .0950	0.0652— .0880
6	0.0666— .0666	0.0666— .0506	0.0506— .0532	0.0426— .0500	0.0488— .0571	0.0523— .0950	<sup>b</sup> 0.2662— .3594
7	0.0666— .0666	0.0666— .0506	0.0506— .0532	0.0426— .0500	0.0488— .0571	0.0523— .0950	0.0652— .0880
8	0.0666— .0666	0.0666— .0506	0.0506— .0532	0.0426— .0500	0.0488— .0571	0.0523— .0950	0.0652— .0880
9	0.0666— .0666	0.0666— .0506	0.0506— .0532	0.0426— .0500	0.0488— .0571	0.0523— .0950	0.0652— .0880
10	0.0666— .0666	0.0466— .0354	0.0354— .0373	0.0426— .0500	0.0488— .0571	0.0523— .0950	0.0652— .0880
11	0.0466— .0466	0.0466— .0354	0.0354— .0373	0.0346— .0407	0.0488— .0571	0.0523— .0950	<sup>b</sup> 0.2662— .3594
12	0.0466— .0466	0.0798— .0798	0.0798— .0798	0.0346— .0407	0.0375— .0439	0.0523— .0950	0.0652— .0880
13	0.0798— .0798	0	0	0.0798— .0798	0.0375— .0439	0.0523— .0950	0.0652— .0880
14	0	0	0	0	0.0798— .0798	0.0366— .0666	0.0466— .0629
15	0	0	0	0	0	0.0366— .0666	0.0466— .0629
16	0	0	0	0	0	0.0798— .1464	0.1464— .1597

<sup>a</sup> Second layer of region I represents the layer that has the reinforcement (see fig. 4).

<sup>b</sup> This represents the thickness of the bead wires.

Table 3. Values of Elastic Constants of Tire Constituents Used in Present Study

Tire constituent	Young's modulus, psi	Shear modulus, psi	Poisson's ratio
Rubber	$4.5 \times 10^2$	$1.51 \times 10^2$	0.49
Nylon cord	$3.5 \times 10^5$	$7.00 \times 10^2$	.66
Bead <sup>a</sup>	$2.9 \times 10^7$	$1.10 \times 10^7$	.30

<sup>a</sup> Since the deformations are small in the bead area, it is reasonable to assume that the bead wires are isotropic.

Table 4. Variation of Nylon Cord End Counts in Different Plies Along Meridian

Ply number (top to bottom)	Cord end count, ends per inch for region—						
	I	II	III	IV	V	VI	VII
1 (tread and sidewall)	Rubber	Rubber	Rubber	Rubber	Rubber	Rubber	Rubber
2	16-16	18-14	14-14	14-14	14-14	14-14	14-14
3	18-18	18-14	14-14	14-14	14-14	14-14	14-14
4	18-18	21-20	20-18	18-16	16-16	16-14	14-14
5	23-21	21-20	20-18	18-16	16-16	16-14	14-14
6	23-21	21-20	20-18	18-16	16-16	16-14	Bead
7-9	23-21	21-20	20-18	18-16	16-16	16-14	14-14
10	23-21	29-26	26-25	18-16	16-16	16-14	14-14
11	30-29	29-26	26-25	25-24	16-16	16-14	Bead
12	30-29	Rubber	Rubber	25-24	24-22	16-14	14-14
13	Rubber			Rubber	24-22	16-14	14-14
14				Rubber	22-22	22-22	
15					22-22	22-22	
16					Rubber	Rubber	

Table 5. Variation of Cord Orientation of Individual Plies,  $\theta_k$ , Along Meridian

Ply number (top to bottom)	$\theta_k$ , deg, for region—						
	I	II	III	IV	V	VI	VII
1	Rubber	Rubber	Rubber	Rubber	Rubber	Rubber	Rubber
2	$\tilde{\theta} - 6$	$\tilde{\theta}$	$\tilde{\theta}$	$\tilde{\theta}$	$\tilde{\theta}$	$\tilde{\theta}$	$\tilde{\theta}$
3	$\tilde{\theta}$	$-\tilde{\theta}$	$-\tilde{\theta}$	$-\tilde{\theta}$	$-\tilde{\theta}$	$-\tilde{\theta}$	$-\tilde{\theta}$
4	$-\tilde{\theta}$	$\tilde{\theta}$	$\tilde{\theta}$	$-\tilde{\theta}$	$-\tilde{\theta}$	$-\tilde{\theta}$	$\tilde{\theta}$
5	$\tilde{\theta}$	$-\tilde{\theta}$	$-\tilde{\theta}$	$\tilde{\theta}$	$\tilde{\theta}$	$\tilde{\theta}$	$-\tilde{\theta}$
6	$-\tilde{\theta}$	$\tilde{\theta}$	$\tilde{\theta}$	$-\tilde{\theta}$	$\tilde{\theta}$	$-\tilde{\theta}$	Bead
7	$\tilde{\theta}$	$-\tilde{\theta}$	$-\tilde{\theta}$	$\tilde{\theta}$	$-\tilde{\theta}$	$\tilde{\theta}$	
8	$-\tilde{\theta}$	$\tilde{\theta}$	$\tilde{\theta}$	$-\tilde{\theta}$	$\tilde{\theta}$	$-\tilde{\theta}$	$\tilde{\theta}$
9	$\tilde{\theta}$	$-\tilde{\theta}$	$-\tilde{\theta}$	$\tilde{\theta}$	$-\tilde{\theta}$	$\tilde{\theta}$	$-\tilde{\theta}$
10	$-\tilde{\theta}$	$\tilde{\theta} + 6$	$\tilde{\theta} + 6$	$-\tilde{\theta}$	$\tilde{\theta}$	$-\tilde{\theta}$	$\tilde{\theta}$
11	$\tilde{\theta} + 6$	$-\tilde{\theta} - 6$	$-\tilde{\theta} - 6$	$\tilde{\theta} + 6$	$-\tilde{\theta}$	$\tilde{\theta}$	Bead
12	$-\tilde{\theta} - 6$	Rubber	Rubber	$-\tilde{\theta} - 6$	$\tilde{\theta} + 6$	$\tilde{\theta}$	
13	Rubber			Rubber	$-\tilde{\theta} - 6$	$-\tilde{\theta}$	$-\tilde{\theta}$
14					Rubber	$\tilde{\theta} + 6$	$\tilde{\theta} + 6$
15						$-\tilde{\theta} - 6$	$-\tilde{\theta} - 6$
16						Rubber	Rubber

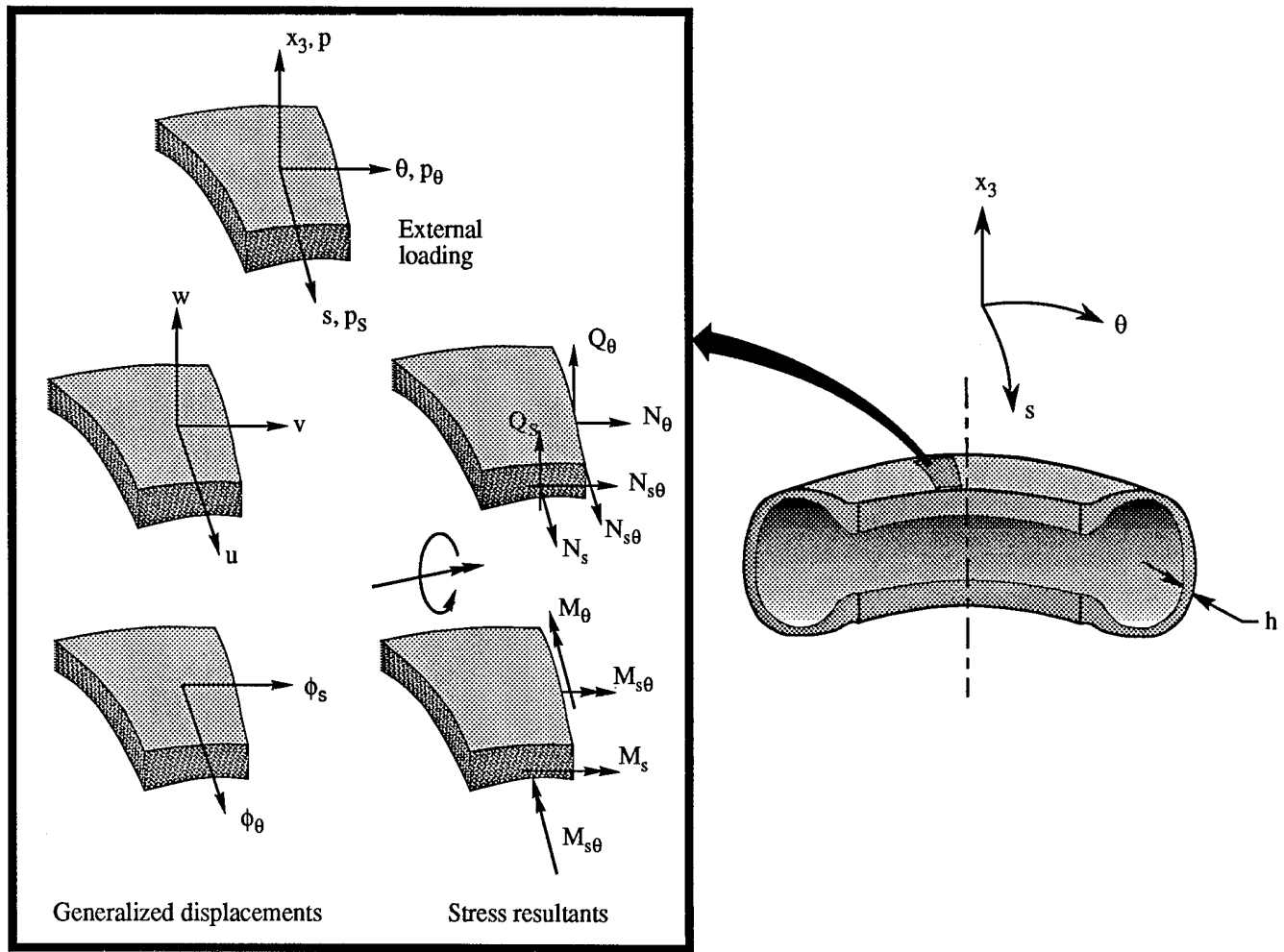


Figure 1. Two-dimensional model of the tire and sign convention for the external loading, generalized displacements, and stress resultants.

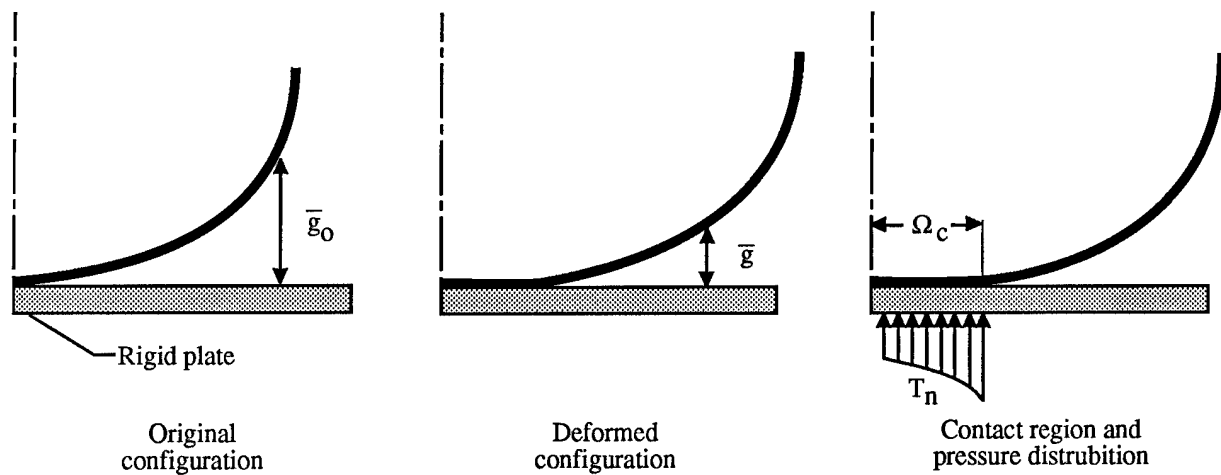


Figure 2. Characteristics of frictionless contact of a shell pressed against a rigid plate.

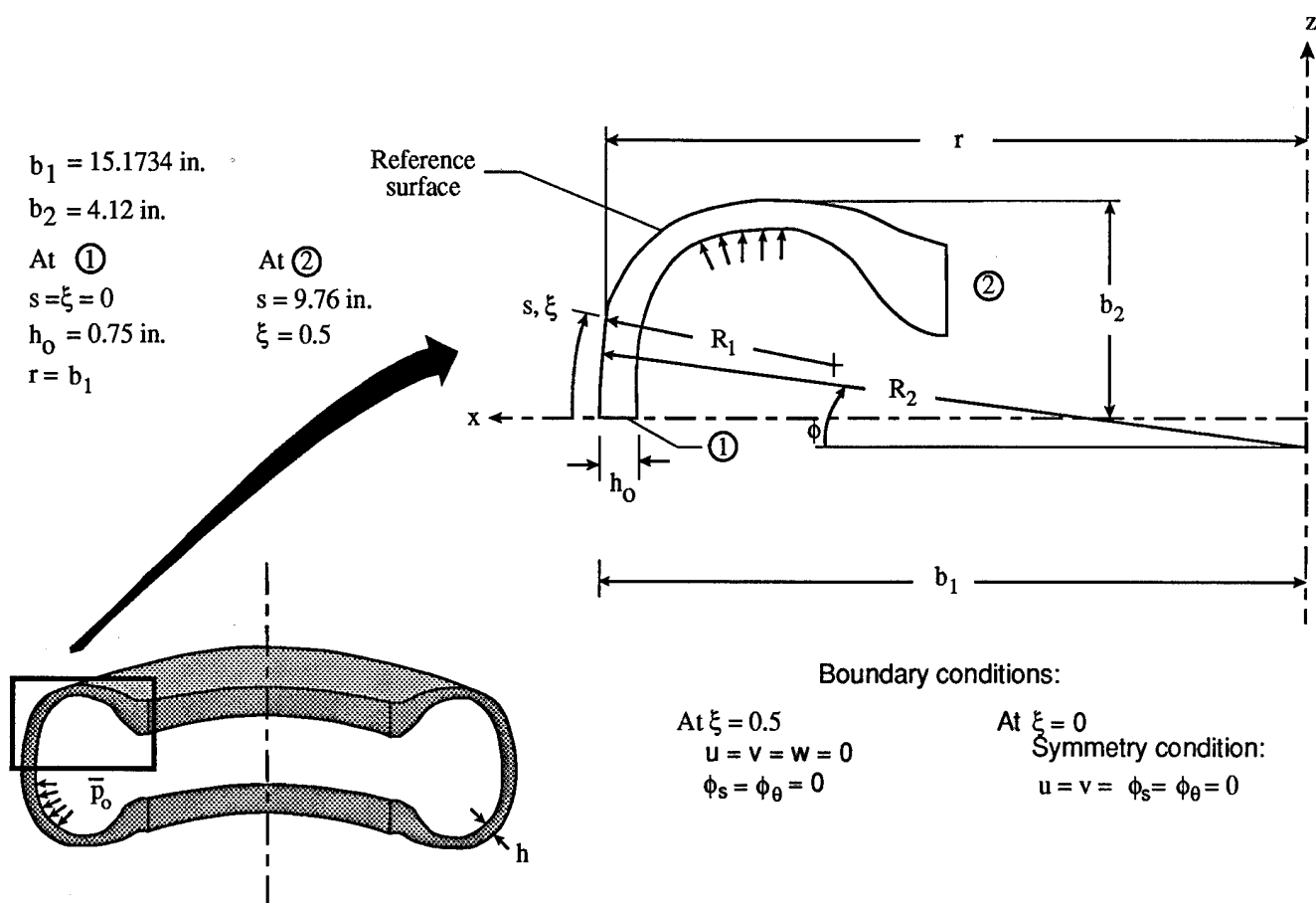


Figure 3. Geometric characteristics of Space Shuttle nose-gear tire.

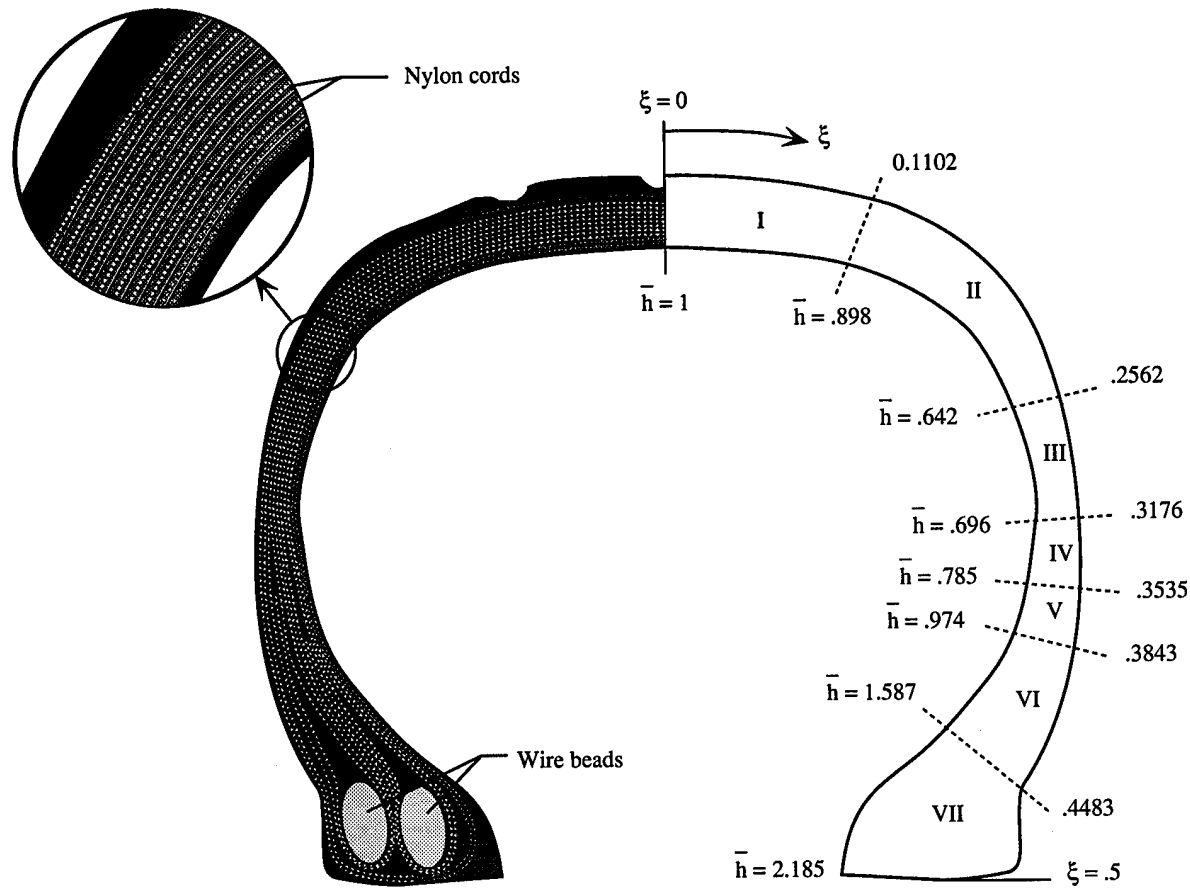


Figure 4. Cross section of Space Shuttle nose-gear tire showing seven model regions.

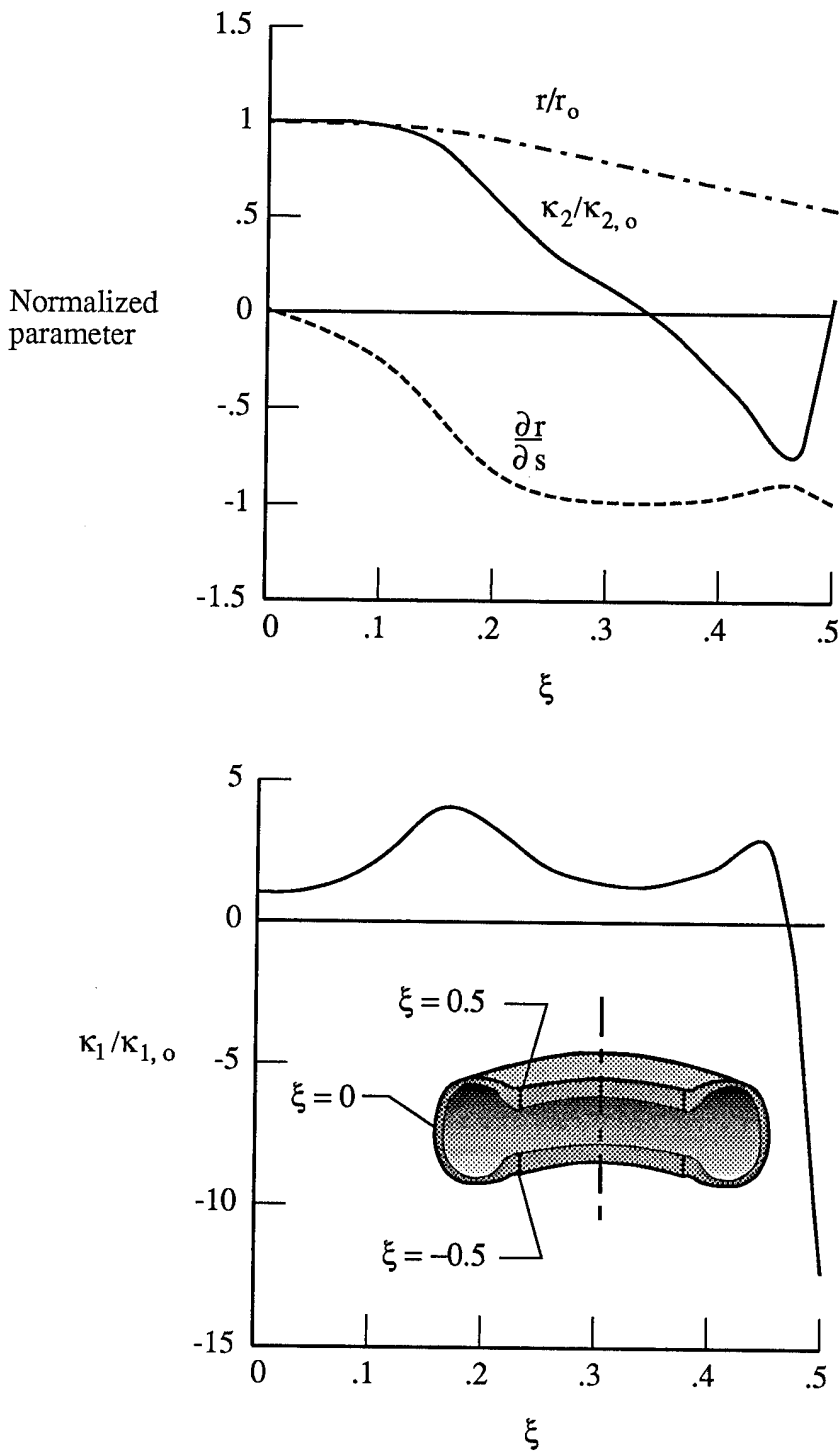
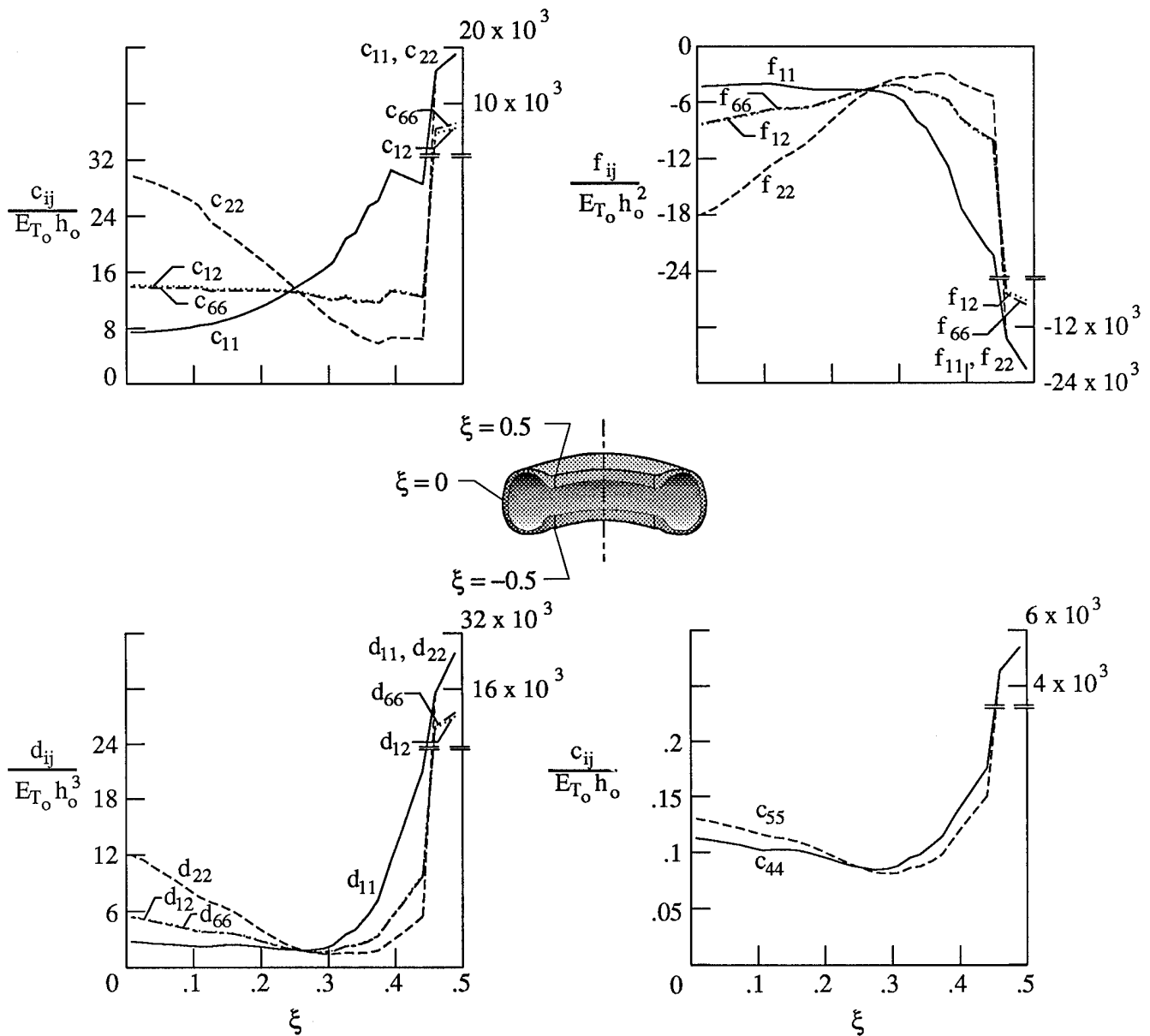
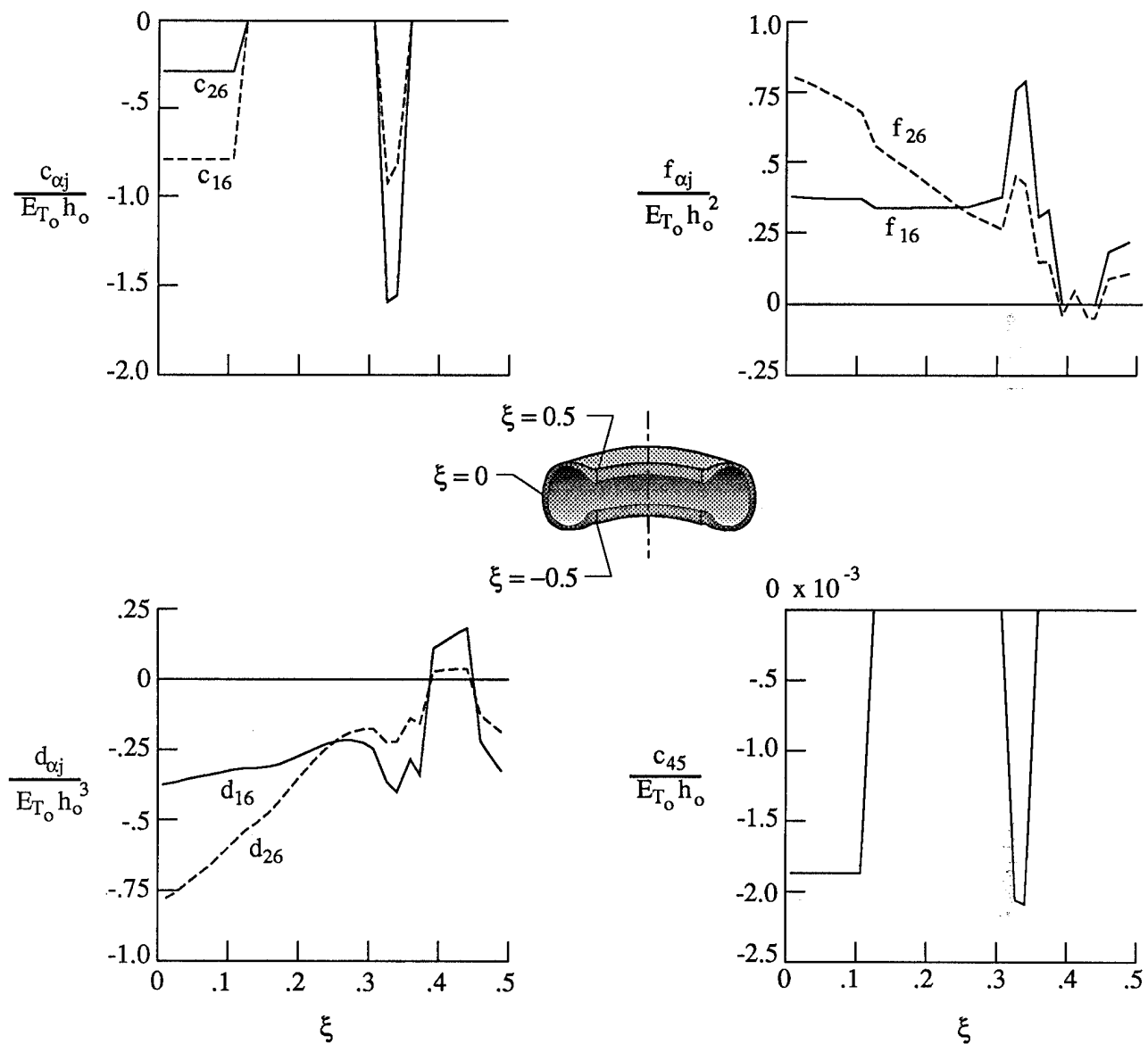


Figure 5. Meridional variation of geometric parameters of two-dimensional shell model of Space Shuttle nose-gear tire. Reference surface chosen to be outer surface.  $r_o = 15.1737$  in.;  $\kappa_{2,o} = 0.0659$  in $^{-1}$ ;  $\kappa_{1,o} = 0.1091$  in $^{-1}$ .



(a) Stiffness coefficients associated with uncoupled (orthotropic) response.

Figure 6. Meridional variation of stiffness coefficients of two-dimensional shell model of Space Shuttle nose-gear tire.  $E_{T_o} = 1160.3$  psi;  $h_o = 0.7513$  in.



(b) Coupling (nonorthotropic) stiffness coefficients.  $\alpha = 1, 2$ .

Figure 6. Concluded.

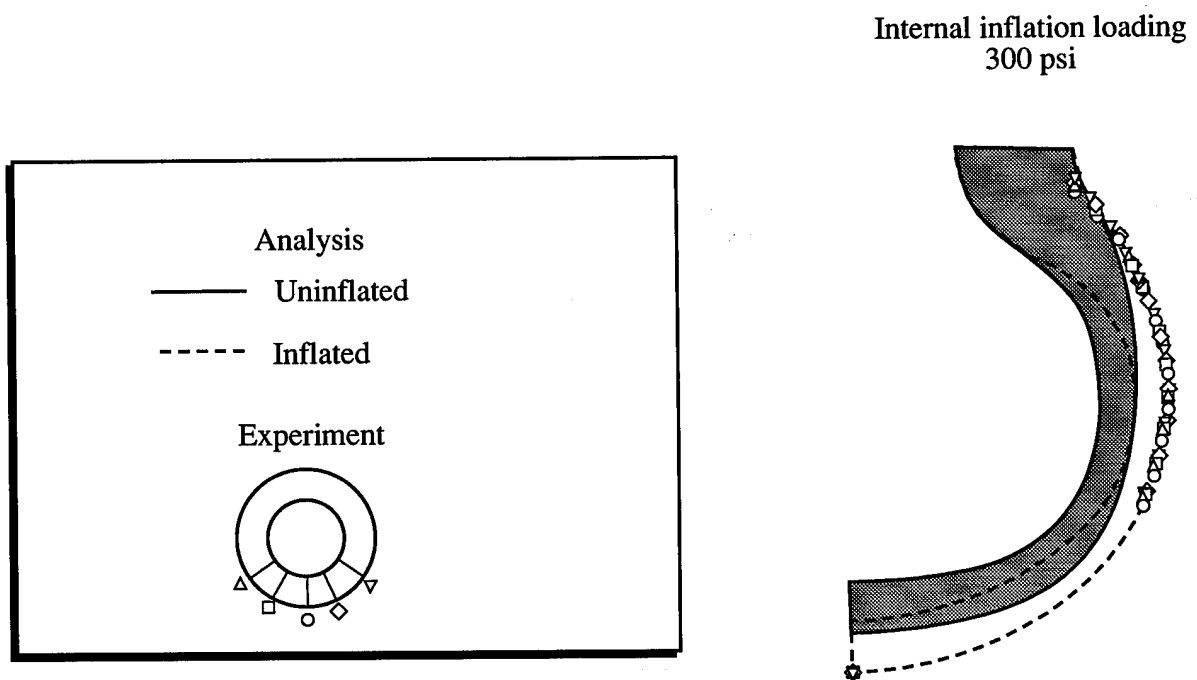
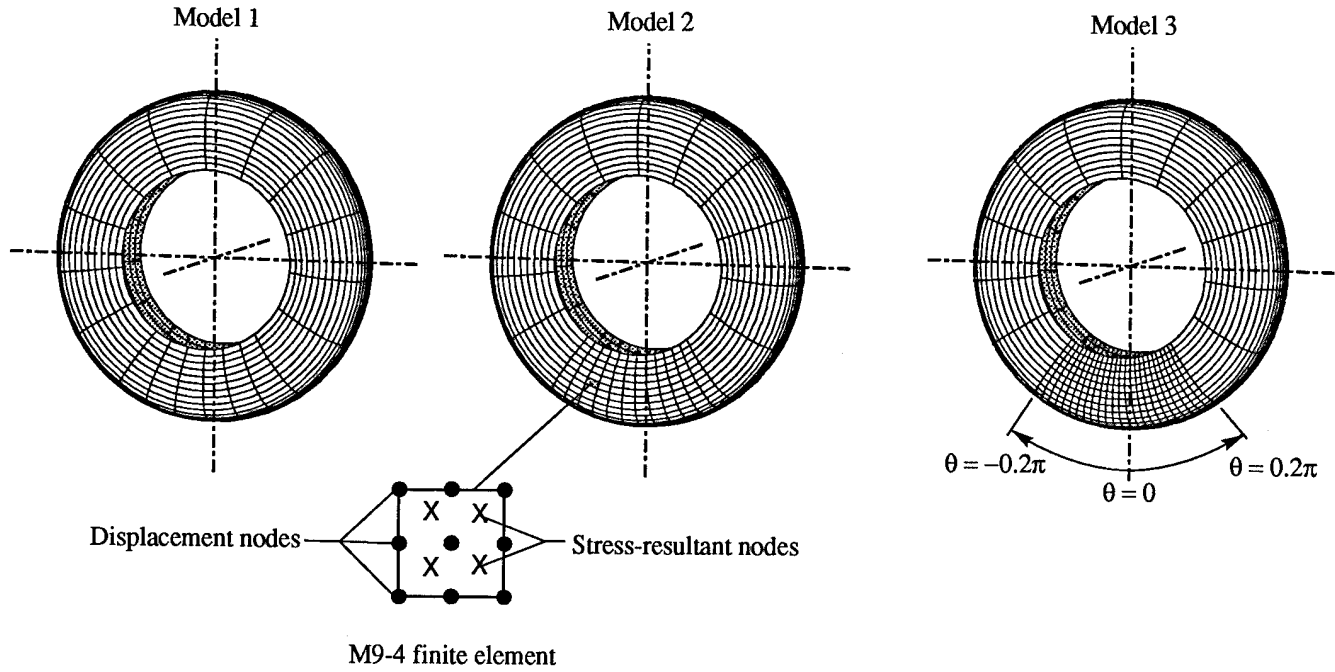


Figure 7. Inflated and uninflated profiles of Space Shuttle nose-gear tire.



Sector	No. of elements (M9-4) for —		
	Model 1	Model 2	Model 3
$-0.2\pi \leq \theta \leq 0.2\pi$	180 ( $30 \times 6$ )	360 ( $30 \times 12$ )	720 ( $30 \times 24$ )
$\theta < -0.2\pi, \theta > 0.2\pi$	360 ( $30 \times 12$ )	360 ( $30 \times 12$ )	360 ( $30 \times 12$ )
Total	540 ( $30 \times 18$ )	720 ( $30 \times 24$ )	1080 ( $30 \times 36$ )

Figure 8. Finite-element models of Space Shuttle nose-gear tire used in present study.

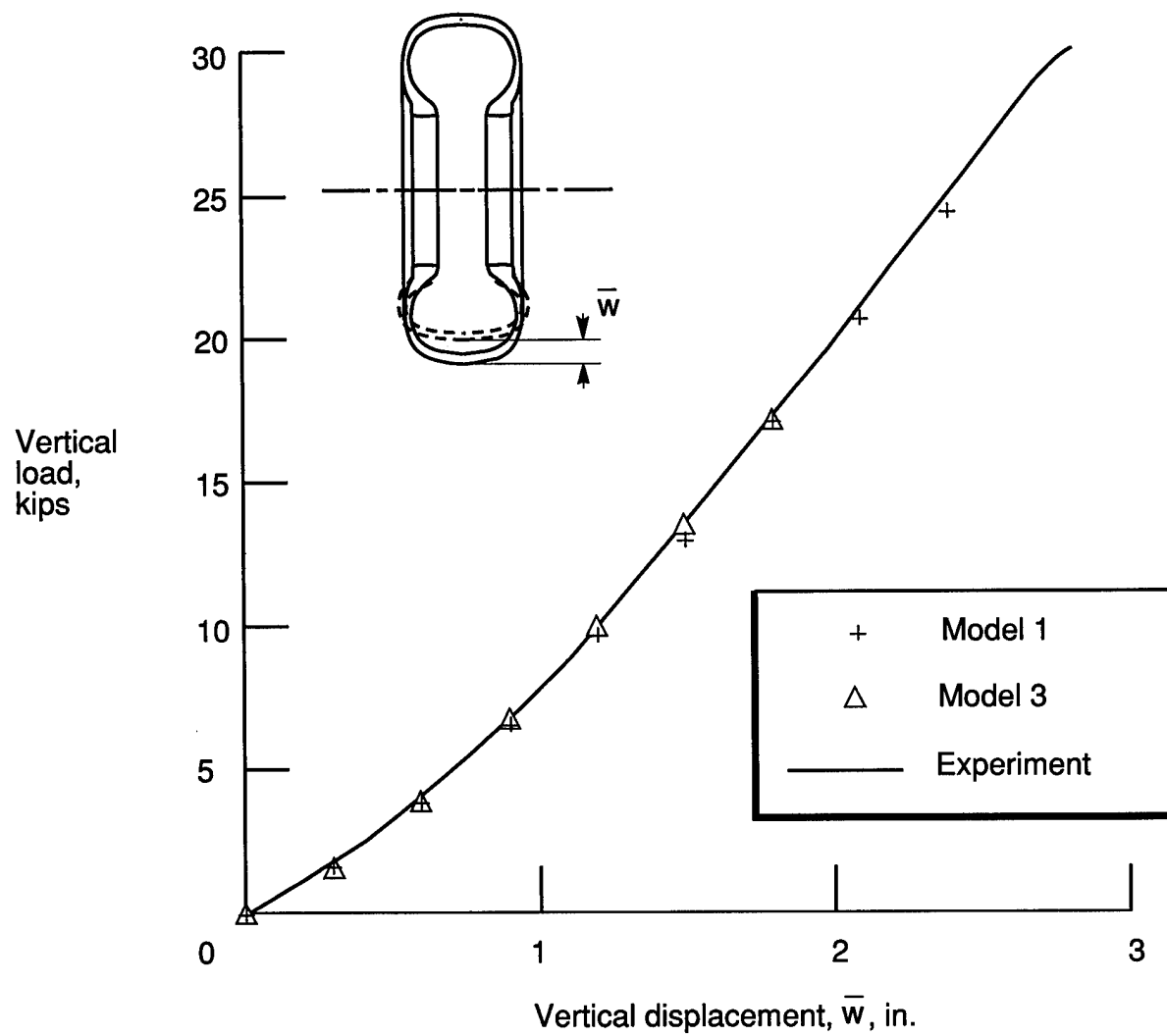


Figure 9. Static vertical load-deflection characteristics of Space Shuttle nose-gear tire.

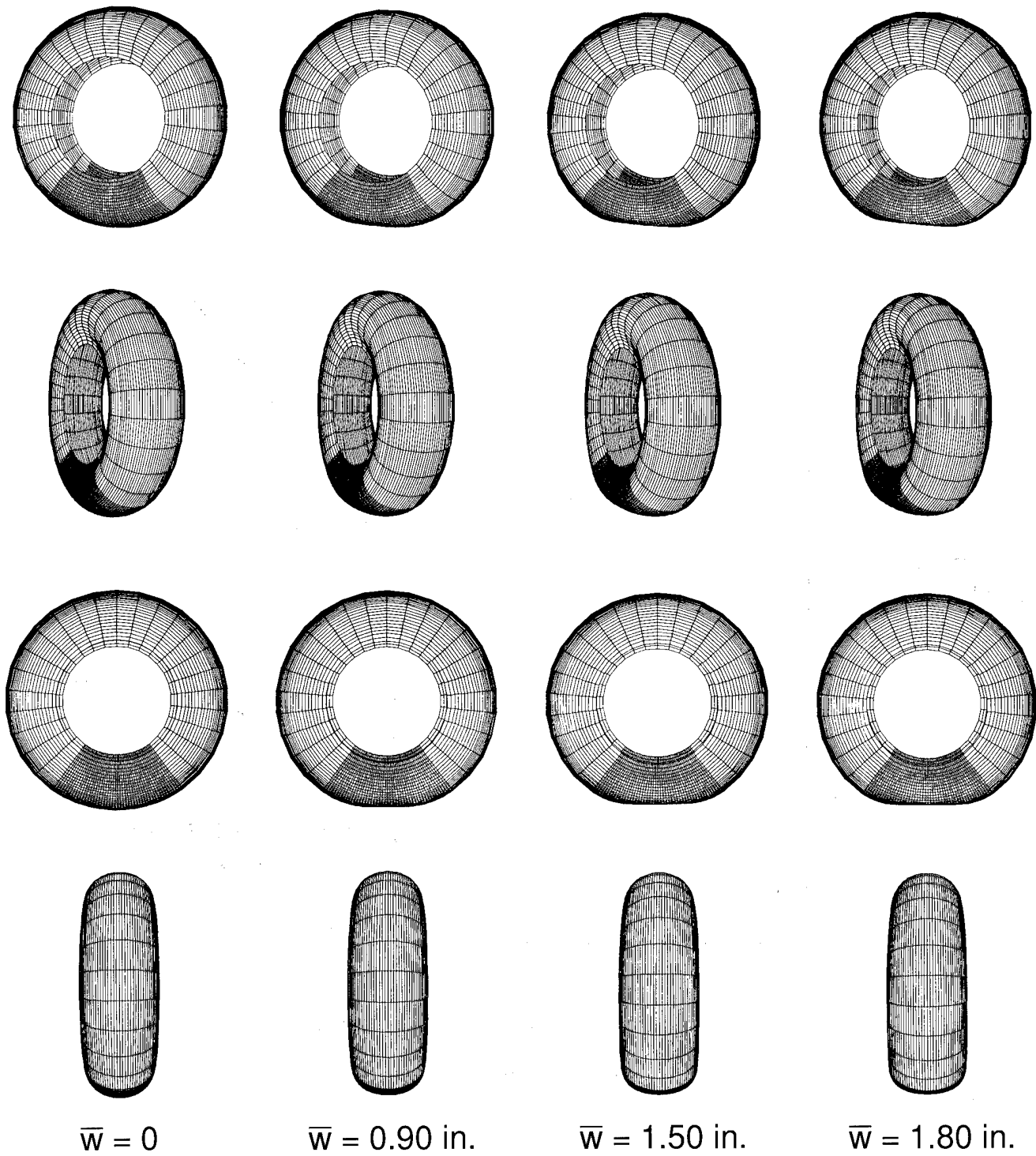


Figure 10. Deformed configurations of Space Shuttle nose-gear tire. The tire is subjected to uniform inflation pressure  $p_o = 300 \text{ psi}$  and is pressed against a rigid pavement.

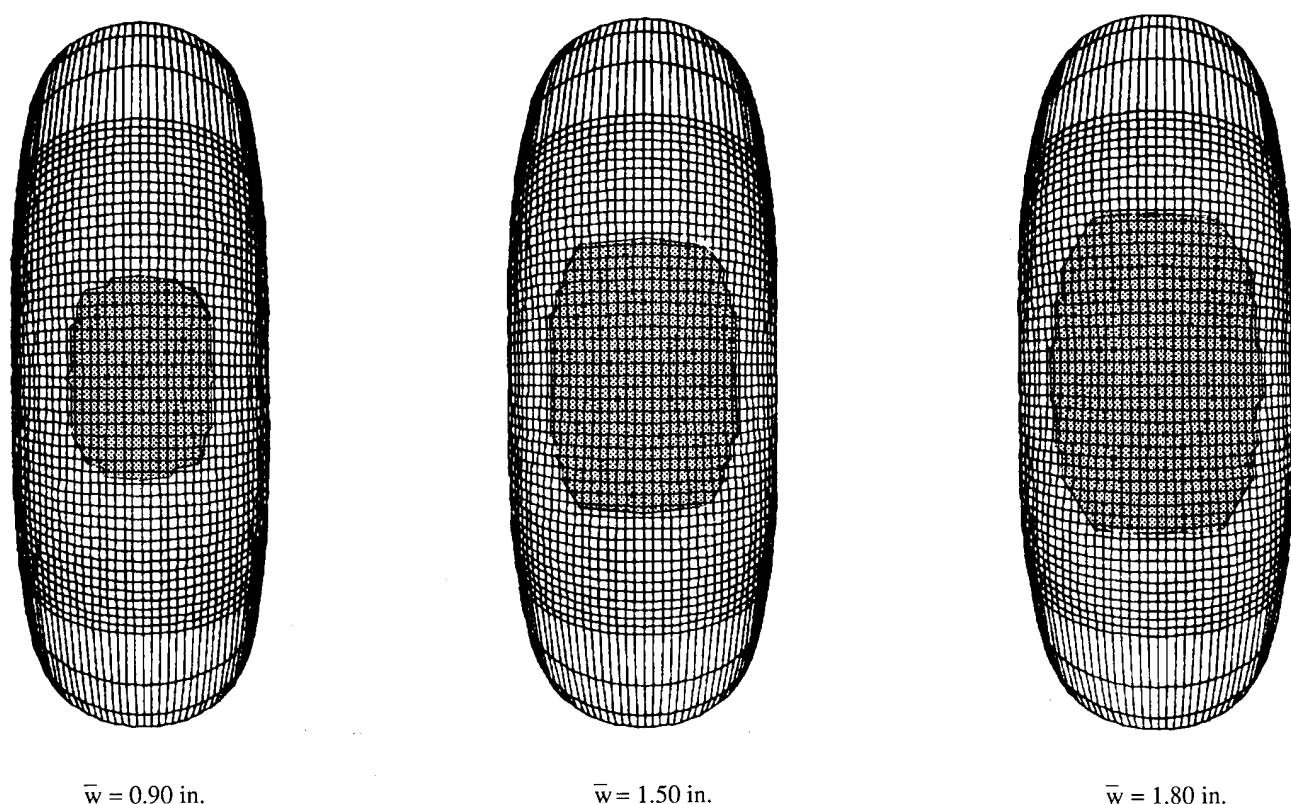


Figure 11. Variation of footprint areas with applied displacements. The tire is subjected to uniform inflation pressure  $p_o = 300$  psi and is pressed against a rigid pavement.

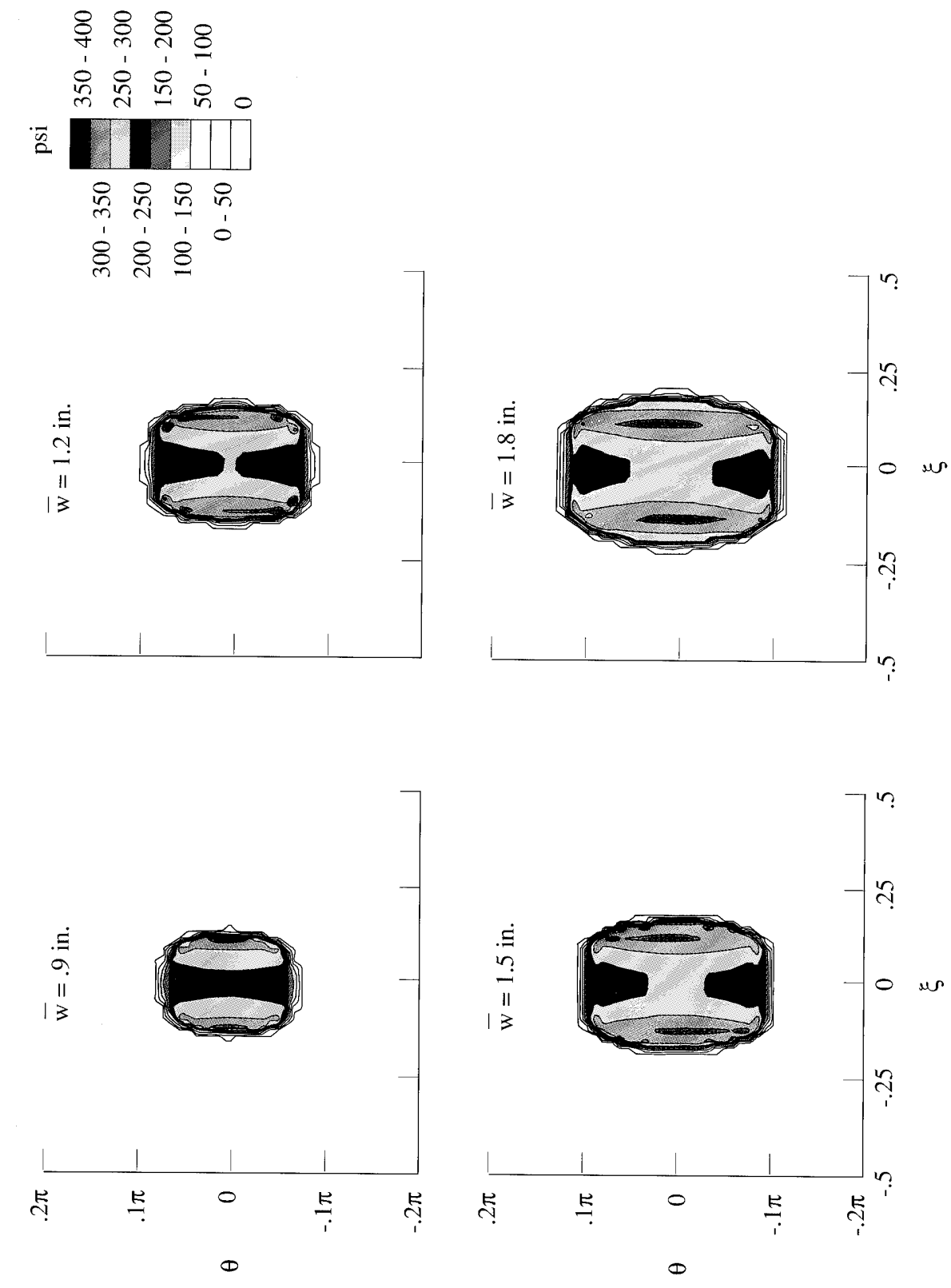


Figure 12. Variation of contact pressure distribution with applied displacements. Space Shuttle nose-gear tire;  $p_o = 300 \text{ psi}$ .

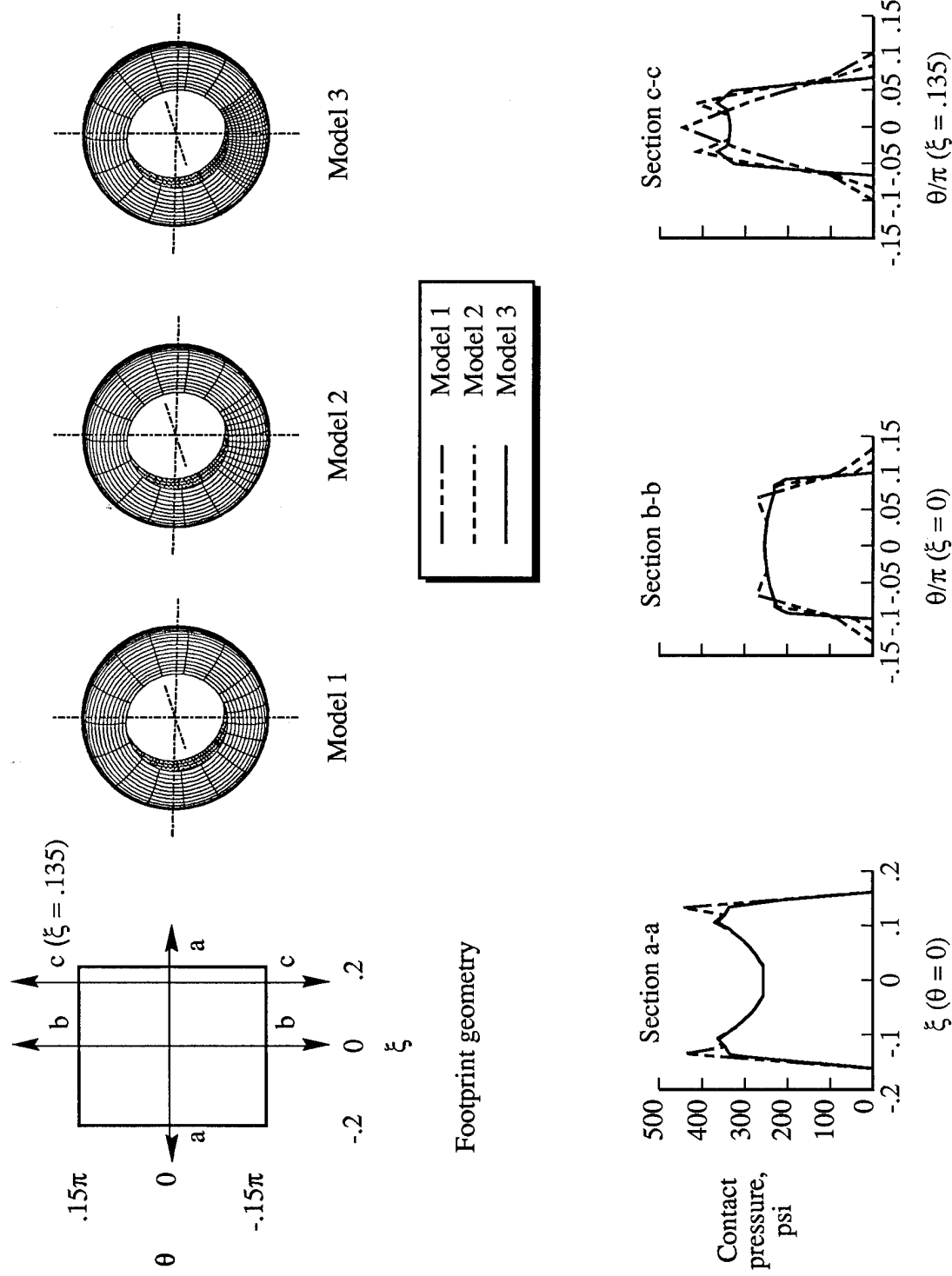


Figure 13. Convergence of contact pressure distribution with mesh refinements. The tire is subjected to uniform inflation pressure  $p_0 = 300$  psi and is pressed against a rigid plate.

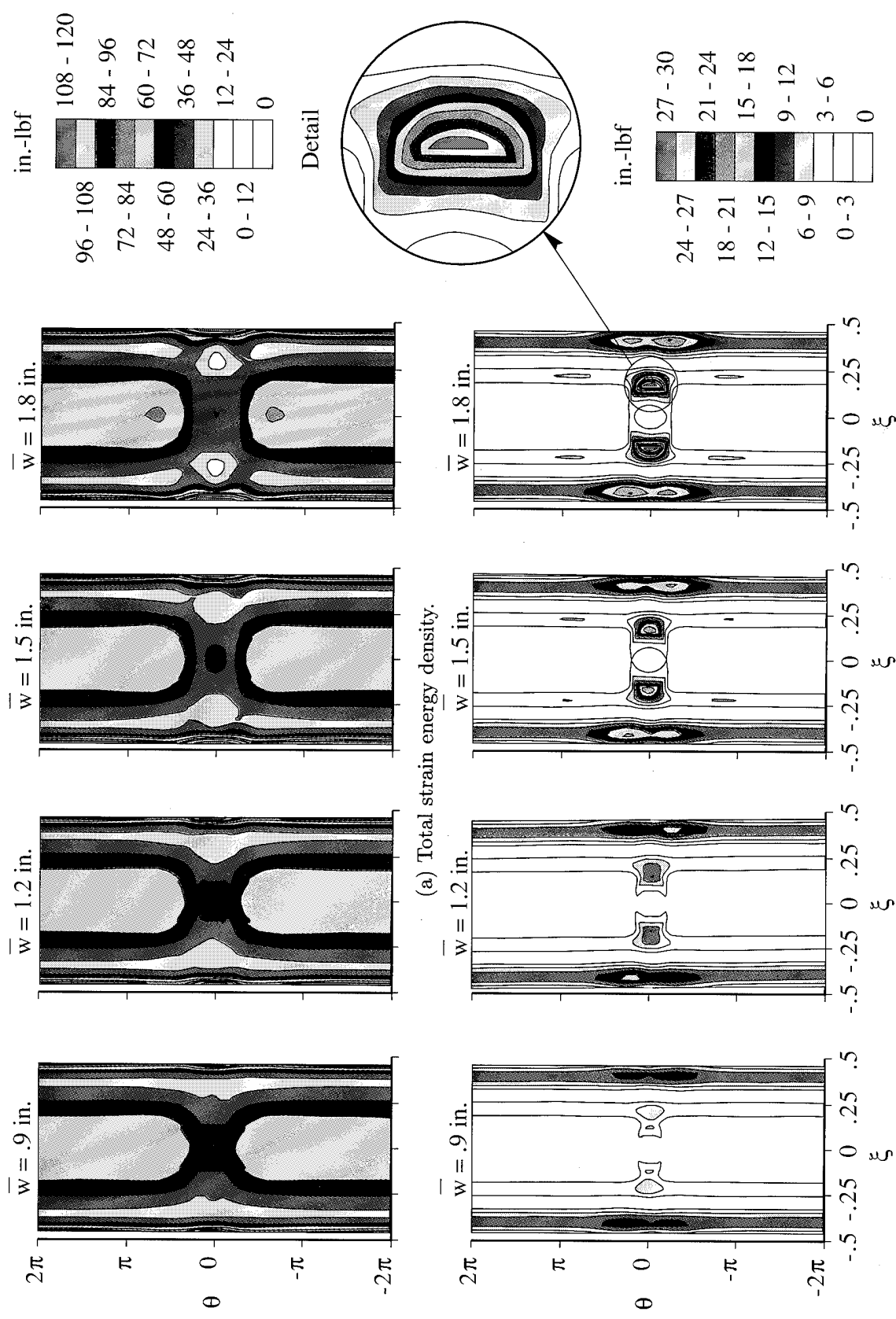


Figure 14. Variation of the strain energy density distribution with applied displacements. Space Shuttle nose-gear tire;  $p_o = 300 \text{ psi}$ .

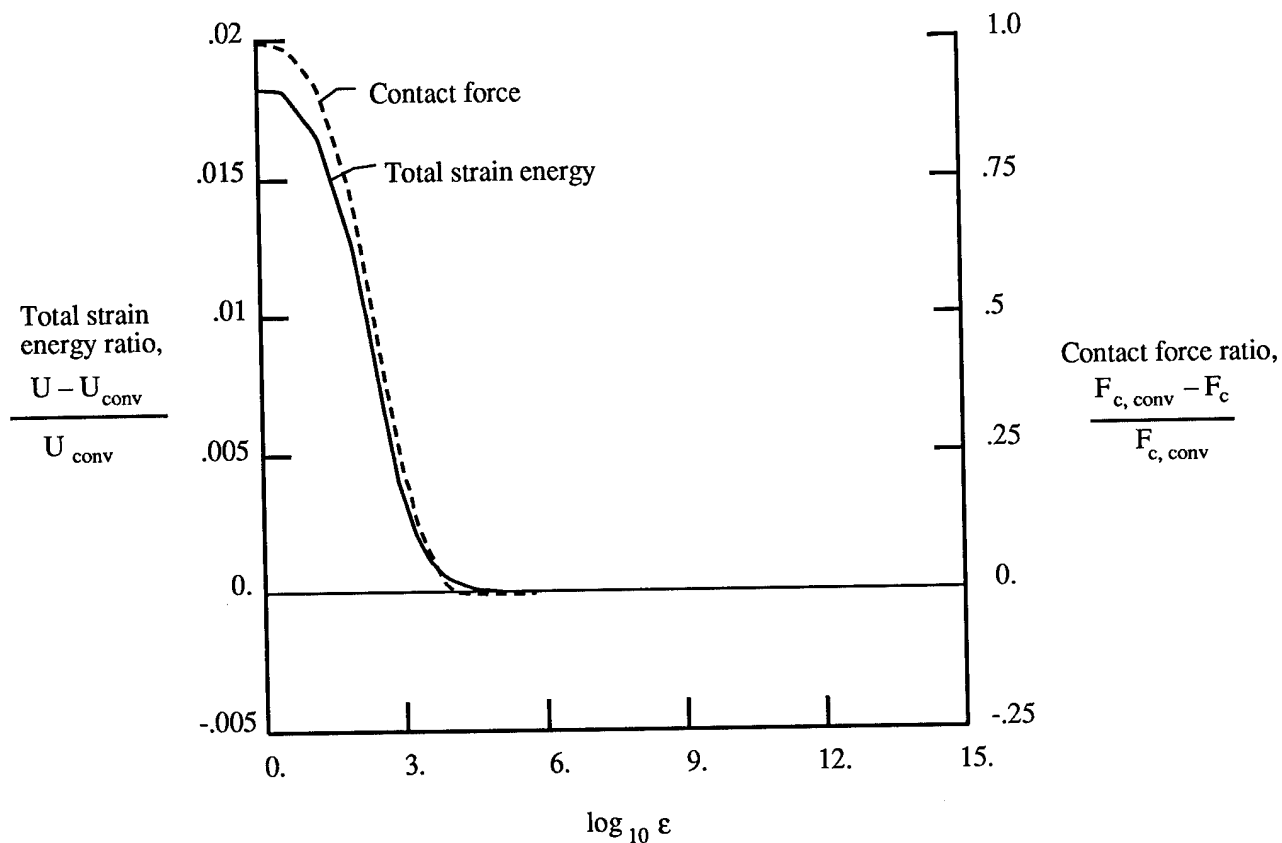


Figure 15. Effect of magnitude of penalty parameter on the accuracy of the total strain energy and the contact force.  $p_o = 300$  psi.



National Aeronautics and  
Space Administration

## Report Documentation Page

1. Report No. <b>NASA TP-3073</b>	2. Government Accession No.	3. Recipient's Catalog No.		
4. Title and Subtitle <b>Computational Methods for Frictionless Contact With Application to Space Shuttle Orbiter Nose-Gear Tires</b>		5. Report Date <b>May 1991</b>		
7. Author(s) <b>Kyun O. Kim, John A. Tanner, Ahmed K. Noor, and Martha P. Robinson</b>		6. Performing Organization Code		
9. Performing Organization Name and Address <b>NASA Langley Research Center Hampton, VA 23665-5225</b>		8. Performing Organization Report No. <b>L-16750</b>		
12. Sponsoring Agency Name and Address <b>National Aeronautics and Space Administration Washington, DC 20546-0001</b>		10. Work Unit No. <b>505-63-41-02</b>		
15. Supplementary Notes <b>Kyun O. Kim: The George Washington University, Joint Institute for Advancement of Flight Sciences, Langley Research Center, Hampton, Virginia. John A. Tanner and Martha P. Robinson: Langley Research Center, Hampton, Virginia. Ahmed K. Noor: Center for Computational Structures Technology, University of Virginia, Langley Research Center, Hampton, Virginia.</b>		11. Contract or Grant No.		
16. Abstract <p>A computational procedure is presented for the solution of frictionless contact problems of aircraft tires. The Space Shuttle nose-gear tire is modeled using a two-dimensional laminated anisotropic shell theory with the effects of variation in material and geometric parameters, transverse-shear deformation, and geometric nonlinearities included. The contact conditions are incorporated into the formulation by using a perturbed Lagrangian approach with the fundamental unknowns consisting of the stress resultants, the generalized displacements, and the Lagrange multipliers associated with the contact conditions. The elemental arrays are obtained by using a modified two-field, mixed variational principle. Numerical results are presented for the Space Shuttle nose-gear tire inflated and pressed against a flat plate. Comparison is made with experiments conducted at NASA Langley Research Center. The detailed information presented herein assists in gaining insight into the structural response of the tire. The numerical studies have demonstrated the high accuracy of the mixed formulation models and the effectiveness of the computational procedure, which combines both the geometrically nonlinear terms and the contact conditions in one iteration loop.</p>				
17. Key Words (Suggested by Author(s)) <b>Frictionless contact Finite elements Mixed models Moderate rotations Nonlinear analysis Tires</b>		18. Distribution Statement <b>Unclassified—Unlimited</b>		
19. Security Classif. (of this report) <b>Unclassified</b>		20. Security Classif. (of this page) <b>Unclassified</b>	21. No. of Pages <b>34</b>	22. Price <b>A03</b>